

2023-01-23

# Water wave interaction with an array of submerged circular plates: Hankel transform approach

Zheng, S

<http://hdl.handle.net/10026.1/20190>

---

10.1103/PhysRevFluids.8.014803

Physical Review Fluids

American Physical Society

---

*All content in PEARL is protected by copyright law. Author manuscripts are made available in accordance with publisher policies. Please cite only the published version using the details provided on the item record or document. In the absence of an open licence (e.g. Creative Commons), permissions for further reuse of content should be sought from the publisher or author.*

Title:

**Water wave interaction with an array of submerged circular plates: Hankel transform approach**

Journal:

**Physical Review Fluids**

Author names and affiliations:

**S. Zheng<sup>1,2</sup>, H. Liang<sup>3,\*</sup>, S. Michele<sup>1</sup>, D. Greaves<sup>1</sup>**

1 School of Engineering, Computing and Mathematics, University of Plymouth, Drake Circus, Plymouth PL4 8AA, United Kingdom

2 State Key Laboratory of Hydrosience and Engineering, Tsinghua University, 100084 Beijing, China

3 Technology Centre for Offshore and Marine, Singapore (TCOMS), 118411, Singapore

\* Email address for correspondence: liang\_hui@tcoms.sg

Accepted 5 January 2023

**Water wave interaction with an array of submerged circular plates:**  
**Hankel transform approach\***

S. Zheng<sup>1,2</sup>, H. Liang<sup>3,\*</sup>, S. Michele<sup>1</sup> and D. Greaves<sup>1</sup>

*1: School of Engineering, Computing and Mathematics,  
University of Plymouth, Drake Circus, Plymouth PL4 8AA, United Kingdom*

*2: State Key Laboratory of Hydroscience and Engineering,  
Tsinghua University, 100084 Beijing, China and*

*3: Technology Centre for Offshore and Marine,  
Singapore (TCOMS), 118411, Singapore*

(Dated: January 23, 2023)

## Abstract

In this paper, water wave interaction with an array of thin submerged horizontal circular plates is investigated within the framework of linear potential flow theory. To consider a more general case, the circular plates studied in this paper are not limited to be rigid and impermeable, and instead, they can be perforated or/and elastic. A Hankel transform approach is employed to formulate integral equations in terms of unknown functions related to the jump in velocity potential across each plate. A Galerkin method is adopted to the solution of these integral equations and the velocity potential jump across the plate is expressed in terms of Fourier-Gegenbauer series, incorporating the known square-root behavior at the edge of the plate in a rapidly convergent numerical scheme. For elastic plates, the plate motion is expanded in modes of free vibration with the edge constraint conditions accounted for intrinsically. The unknown coefficients of the plate motion are further expressed in terms of the unknown coefficients related to the velocity potential jump. The Hankel transform based model is found to be valid for multiple plates distributed arbitrarily, including the staggered arrangement, for which the traditional eigenfunction matching method would not work. In-depth discussions have been made to the hydrodynamic responses of staggered arrangement of plates. It is found that the staggered arrangement of plates can result in notable wave focusing, while less energy dissipation. The largest principal strain is observed on the front region of the plate submerged at a shallower depth.

**Keywords:** submerged circular plates; Hankel transform approach; water waves

---

\* [liang\\_hui@tcoms.sg](mailto:liang_hui@tcoms.sg)

## I. INTRODUCTION

The interaction of linear water waves with plates of small thickness has received considerable research attention. Possible utilization of such a structure for purposes including but not limited to mitigating severe wave attack on offshore/coastal facilities and absorbing/dissipating wave power is promising. Impermeable rigid plate can be used as a wave lens to amplify wave energy [1], and a heave plate to suppress violent resonant wave frequency motion of an offshore platform [2]. Resonance of plate bending elastic modes has been proven to be an effective power extraction mechanism in [3], whereas more recently Michele *et al.* [4] and Zheng *et al.* [5] solved the case of a floating free-edge flexible circular wave energy converter by means of free-edge dry modes expansion and dispersion relation for flexural wave propagation, respectively. Liang *et al.* [6] considered wave effects on submerged perforated elastic plates numerically by coupling a boundary element method and dry modes of plates. Elastic perforated plates have potential to be used as a power take-off device to harness wave power and membrane-type photovoltaic panels [7]. In addition, an elastic plate is also widely used to model natural structures, for example: sea ice, stingray, etc [8, 9].

The interactions between water waves and submerged circular plates have been extensively studied because of their potential practical significance as well as theoretical interests. Apart from experimental and numerical studies, analytical methods have been adequately developed hitherto. Among various analytical models, the eigenfunction matching method has been widely applied to deal with the interaction between water waves and a circular plate [10], and multiple plates can be considered by using Graf's addition theorem [11, 12]. Despite the fact that significant progress has been achieved, this method has several limitations. First, the square-root singularity at the edge of the plate is usually disregarded in the eigenfunction matching method. As a consequence, a large number of terms are required to achieve converged results. Secondly, it is difficult to apply to deep water problems due to the fact that the convergence of the expansion series underneath the plate is slow when water depth is large. Thirdly, if the plates are perforated and/or elastic, complex dispersion equations will be encountered with the eigenfunction matching method. However, it is a big challenge to find all the complex roots over a range of parameters, although several methods for solving the complex dispersion equations have been proposed [e.g., see 10, 13, 14]. Last but not least, to the best of the authors' knowledge, the traditional eigenfunction matching method would end up in some amount of difficulty when the plates overlap horizontally, e.g., see the staggered

arrangement as shown in Fig. 1, particularly due to the non-circular regions encountered in the fluid domain dividing scheme. A variant of the eigenfunction matching method is the modified residue calculus method, in which the specific behavior at the edges of the plate can be accounted for. Readers are referred to [15] for a detailed description of this method.

In contrast to the popular eigenfunction matching method, the Hankel transform approach [16, 17] does not suffer from the aforementioned difficulties. In essence, the Hankel transform approach amounts to the Galerkin boundary integral method [18]. It adopts the free-surface Green function as the fundamental solution to the Laplace equation although not explicitly expressed, and different types of free-surface Green functions have been thoroughly collected in [19]. This feature enables the method to account for the deep water problem and without the need to find the complex roots. By selecting proper basis functions, the square-root singularity can be incorporated leading to rapid convergence [17, 20, 21]. Moreover, this approach can be generalized to consider interactions among water waves, current and plates as long as the proper free-surface Green function is used [22]. Other methods, e.g., the Fourier transforms-based method [17] and the Wiener-Hopf technique [23], which also avoid the need to find the roots of the highly non-trivial dispersion equations, were applied in solving the two-dimensional problems of water-wave scattering by infinitely-long plates of constant width, and semi-infinite submerged thin elastic or poroelastic plates.

The present paper is focused on the problem of water wave interaction with an array of submerged circular plates. Basically, the distribution of an array of submerged plates can be classified into three types: coaxial arrangement, side by side arrangement, and staggered arrangement (i.e., overlap laterally) (see Fig. 1). Motivated by the desire to study the hydrodynamics of an arbitrary arrangement of multiple plates, a Hankel transform based model is proposed in this paper. A Galerkin method is applied to the solution of the integral equations to ensure that the behavior of the fluid velocity at the edges of the plates is captured accurately. The plates in the present model are not limited to being rigid and impermeable, and instead they can be perforated or/and elastic, making the model applicable to a wider range of applications. Moreover, the present model enables us to investigate hydrodynamic responses of plates in a staggered or coaxial configuration.

As a follow-up to authors' previous work [6, 12], the focus of the present study is mainly placed on the hydrodynamic responses of two disks in a staggered configuration, which has been seldom considered in the literature. Besides the wave exciting forces, energy dissipation, hydroelastic deflections, and free surface patterns, we also considered the velocity field and the distribution

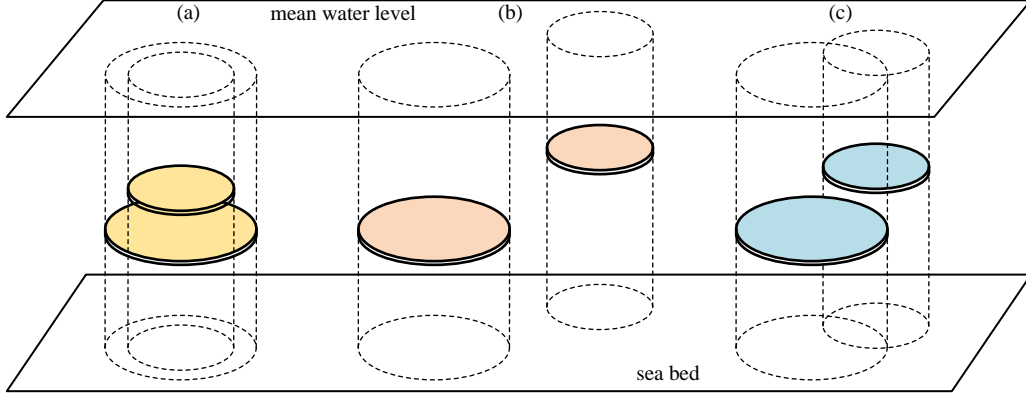


FIG. 1: Sketch of three arrangements of a pair of submerged circular plates: (a) coaxial arrangement; (b) side by side arrangement; (c) staggered arrangement.

of principal strain. It is unraveled that the staggered arrangement of plates can result in notable wave focusing, while less energy dissipation, and the largest principal strain is observed on the front region of the plate submerged at a shallower depth. Our present model is focused on wave interaction with plates of clamped edges or simply supported edges, and it can be easily extended to the case of free-edge plates.

The remainder of this paper is structured as follows: Sec. II describes the basic Hankel transform-based mathematical model. Sec. III presents the theoretical expressions of the velocity potential jump across the plates and the deformation of the plates should they be flexible. Moreover, the linear algebraic system for evaluating unknown coefficients and also the expressions of the free-surface elevation, wave excitation forces, and wave power dissipation are derived. Sec. IV supplies the model validation. A multiparameter study is carried out with the validated model, the results of which and the corresponding discussions are reported in Sec. V. Finally, the conclusions are outlined in Sec. VI.

## II. MATHEMATICAL MODEL

Water wave interaction with an array of  $N$  submerged horizontal circular thin plates is considered. The water is of constant depth  $h$  and the  $n$ th circular plate is of radius  $R_n$  with submergence  $d_n$ . The definition of the coordinate systems follows from that of [12] (see Fig. 2) though we treat the problem with a different approach. There is a global Cartesian coordinate system  $Oxyz$  and  $N$  plate associated local cylindrical coordinate systems  $O_n r_n \theta_n z$  centered on the origin of the  $n$ th

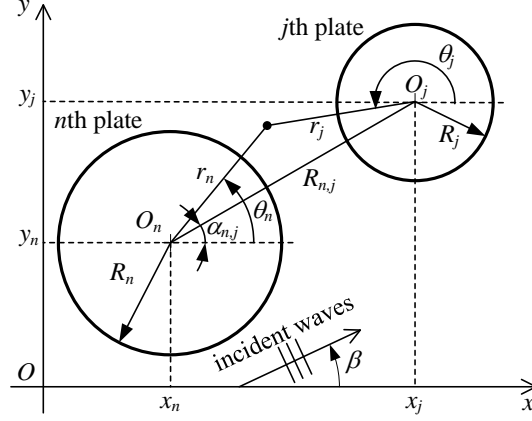


FIG. 2: Definition of the coordinate systems (top view) (after [12]).  $R_{n,j}=0$ ,  $R_{n,j} \geq R_n + R_j$  and  $0 < R_{n,j} < R_n + R_j$  correspond to the coaxial arrangement, side by side arrangement, and staggered arrangement, respectively (see Fig. 1).

circular plate for  $n = 1, \dots, N$ . In addition, a global cylindrical coordinate system  $Or_0\theta_0z$  (not plotted in Fig. 2) is defined with its origin coinciding with the Cartesian coordinate system. The mean water level coincides with the plane  $z = 0$  with the axis  $z$  pointing upwards. The horizontal position of  $O_n$  in the Cartesian coordinate system is  $(x_n, y_n)$ . The plates are subjected to incident plane waves of amplitude  $A$  and angular frequency  $\omega$  propagating at a heading angle  $\beta$  with respect to the  $Ox$  direction.

It is assumed that both the free-surface steepness and plate motion are small enough so that linear theory applies and the fluid is inviscid, incompressible and its motion is irrotational. The governing equation to be satisfied by the velocity potential  $\phi$  in the fluid domain is

$$\nabla^2 \phi = 0, \quad (1)$$

where  $\nabla^2$  denotes the three-dimensional Laplacian.

The velocity potential may be divided into two components as

$$\phi = \phi_I + \phi_D, \quad (2)$$

where  $\phi_I$  denotes the undisturbed incident wave velocity potential, and  $\phi_D$  is the diffracted velocity potential.

The incident wave potential  $\phi_I$  that satisfies the Laplace's equation and the boundary conditions on the free-surface and seabed can be expressed in the global Cartesian coordinate system  $Oxyz$  as



[e.g., see 15]

$$\phi_I(x, y, z) = -\frac{igA}{\omega} Z(z) e^{ik(x \cos \beta + y \sin \beta)}, \quad \text{with } Z(z) = \begin{cases} \frac{\cosh[k(z+h)]}{\cosh(kh)}, & \text{(finite depth)} \\ e^{Kz}, & \text{(infinite depth)} \end{cases} \quad (3)$$

where  $g$  is the acceleration due to gravity, and  $k \in \mathbb{R}^+$  the wavenumber, satisfying the dispersion relation  $\omega^2/g \equiv K = k \tanh(kh)$ . In the case of infinite depth, the dispersion relation holds in the limit  $h \rightarrow \infty$  giving  $K = k$ . By using Jacobi-Anger expansion, the incident wave potential  $\phi_I$  in the local cylindrical coordinate systems  $O_n r_n \theta_n z$  is equivalently written as [e.g., see 11]

$$\phi_I(r_n, \theta_n, z) = -\frac{igA}{\omega} Z(z) e^{ik(x_n \cos \beta + y_n \sin \beta)} \sum_{m=-\infty}^{\infty} i^m e^{-im\beta} J_m(kr_n) e^{im\theta_n}, \quad (4)$$

where  $J_m$  denote the  $m$ th order Bessel functions of the first kind.

The diffracted potential  $\phi_D$  may be written as

$$\phi_D = \sum_{n=1}^N \sum_{m=-\infty}^{\infty} \phi_{n,m}(r_n, z) e^{im\theta_n}, \quad (5)$$

in which  $\phi_{n,m}$  satisfies the Laplace equation in cylindrical coordinates,

$$\left( \frac{\partial^2}{\partial r_n^2} + \frac{1}{r_n} \frac{\partial}{\partial r_n} - \frac{m^2}{r_n^2} + \frac{\partial^2}{\partial z^2} \right) \phi_{n,m} = 0, \quad (6)$$

the free surface boundary condition

$$\left( \frac{\partial}{\partial z} - K \right) \phi_{n,m} = 0, \quad z = 0, \quad (7)$$

the boundary condition at the seabed

$$\frac{\partial \phi_{n,m}}{\partial z} = 0, \quad z = -h, \quad \text{or} \quad |\nabla \phi_{n,m}| = 0, \quad z \rightarrow -\infty, \quad (8)$$

depending on whether the fluid is finite or infinite depth, and the Sommerfeld radiation condition at  $r_n \rightarrow \infty$ .

The continuity of vertical velocity and the kinematic boundary conditions at the  $n$ th plate for  $n = 1, 2, \dots, N$  [e.g., see 12]

$$\frac{\partial \phi_I}{\partial z} + \frac{\partial \phi_D}{\partial z} = \frac{\partial \phi_n^+}{\partial z} = \frac{\partial \phi_n^-}{\partial z} = -ip_n (\phi_n^+ - \phi_n^-) - i\omega \eta_n, \quad z = -d_n, 0 < r_n < R_n \quad (9)$$

should also be satisfied, where  $p_n$  denotes a complex porosity parameter of the  $n$ th plate [e.g., see 24], whose real and imaginary parts represent the resistance and inertial effects, respectively.

$\phi_n^+ = \phi|_{z=-d_n^-}$  and  $\phi_n^- = \phi|_{z=-d_n^+}$  denote the velocity potentials above and below the  $n$ th circular plate, respectively.  $\eta_n$  represents the deformation of the  $n$ th plate and  $\eta_n = 0$  if the plate is rigid and with its edge fixed. Eq. (9) states that the jump in pressure across the plate is proportional to the velocity of the fluid relative to the velocity of the plate. The imaginary part of  $p_n$  encodes a phase lag in this flow law, and  $p_n = 0$  if the plate is impermeable. When  $p_n \rightarrow \infty$ , the plate has a vanishing effect since Eq. (9) implies not only the continuity of the vertical velocity but also the continuity of the velocity potential (i.e.,  $\phi_n^+ - \phi_n^- = 0$ ).

The jump in the velocity potential across  $z = -d_n$  may be written as

$$\phi_n^+ - \phi_n^- = \begin{cases} \sum_{m=-\infty}^{\infty} P_{n,m}(r_n) e^{im\theta_n}, & r_n \leq R_n \\ 0, & r_n > R_n \end{cases}, \quad (10)$$

where  $P_{n,m}(r_n)$  can be further expanded into a series of basis functions, which will be given in Sec. III.

When the plate is flexible, in addition to the above governing equation and boundary conditions, the dynamic boundary conditions on the  $n$ th circular plate for  $n = 1, 2, \dots, N$

$$g(\chi_n \Delta^2 - K \gamma_n) \eta_n + i\omega(\phi_n^+ - \phi_n^-) = 0, \quad (11)$$

should be satisfied [e.g., see 12, 25], in which  $\Delta$  denotes the Laplacian operator in the horizontal plane.  $\chi_n$  and  $\gamma_n$  represent the flexural rigidity and the mass per unit area of the plate, respectively, scaled with respect to the water density. The detailed definitions of those parameters can be found in [11, 12]. For simply supported flexible plates, we have vanishing of bending moment and displacement at the edges. While, in the case of flexible plates having clamped edges, both displacement and slope vanish at the edges. The expression of  $\eta_n$  will be given in Sec. III B.

Following [17], the Hankel transform of  $\phi_{n,m}$  is defined by

$$\bar{\phi}_{n,m}(\alpha, z) = \int_0^\infty r_n \phi_{n,m}(r_n, z) J_m(\alpha r_n) dr_n, \quad (12)$$

with inverse

$$\phi_{n,m}(r_n, z) = \int_0^\infty \alpha \bar{\phi}_{n,m}(\alpha, z) J_m(\alpha r_n) d\alpha. \quad (13)$$

Taking Hankel transforms of Eqs. (6)-(8) and (10) gives rise to

$$\left( \frac{\partial^2}{\partial z^2} - \alpha^2 \right) \bar{\phi}_{n,m} = 0, \quad (14)$$

$$\left(\frac{\partial}{\partial z} - K\right)\bar{\phi}_{n,m} = 0, \quad z = 0, \quad (15)$$

$$\frac{\partial \bar{\phi}_{n,m}}{\partial z} = 0, \quad z = -h, \quad \text{or} \quad \bar{\phi}_{n,m} \rightarrow 0, \quad z \rightarrow -\infty, \quad (16)$$

depending on whether the fluid is finite or infinite depth, and

$$\bar{\phi}_{n,m}(\alpha, -d_n^-) - \bar{\phi}_{n,m}(\alpha, -d_n^+) = \int_0^{R_n} r_n P_{n,m}(r_n) J_m(\alpha r_n) dr_n \equiv \bar{P}_{n,m}(\alpha). \quad (17)$$

It is assumed in what follows that the fluid is of finite depth and we comment later on the changes required for infinite depth.

It should be noted that  $\phi_{n,m}(r_n, z)$  have a continuous  $z$ -derivative at  $z = -d_n$  for all  $r_n$ , resulting in

$$\frac{\partial}{\partial z} \bar{\phi}_{n,m}(\alpha, -d_n^-) = \frac{\partial}{\partial z} \bar{\phi}_{n,m}(\alpha, -d_n^+). \quad (18)$$

On account of  $\bar{\phi}_{n,m}$  satisfying Eqs. (14)-(18) and applying the method of separation of variables, we have

$$\bar{\phi}_{n,m}(\alpha, z) = \bar{P}_{n,m}(\alpha) f_n(\alpha, z), \quad (19)$$

where

$$f_n(\alpha, z) = \begin{cases} \frac{\sinh[\alpha(h-d_n)][\alpha \cosh(\alpha z) + K \sinh(\alpha z)]}{\alpha \sinh(\alpha h) - K \cosh(\alpha h)}, & -d_n \leq z \leq 0 \\ \frac{\cosh[\alpha(z+h)][-\alpha \sinh(\alpha d_n) + K \cosh(\alpha d_n)]}{\alpha \sinh(\alpha h) - K \cosh(\alpha h)}, & -h \leq z \leq -d_n \end{cases}. \quad (20)$$

There is a pole on the positive real  $\alpha$ -axis at  $\alpha = k$ , for which the denominator of  $f_n(\alpha, z)$  equals zero given the dispersion relation  $K = k \tanh(kh)$ . For the thin plate located on the seabed, i.e., when  $d_n \rightarrow h$ , we have  $f_n(\alpha, z) \rightarrow 0$  and  $\partial f_n(\alpha, z)/\partial z \rightarrow 0$  for  $-h < z \leq 0$ , meaning that the diffracted velocity potentials turn to vanish as expected.

Taking inverse transforms of the representation in Eq. (19) using Eq. (13) gives

$$\phi_{n,m}(r_n, z) = \int_0^\infty \alpha \bar{P}_{n,m}(\alpha) f_n(\alpha, z) J_m(\alpha r_n) d\alpha. \quad (21)$$

To ensure that the diffracted waves are outgoing, the contour of integration is defined to bypass the pole  $\alpha = k$  from below [17].

$$\phi_{n,m}(r_n, z) = \oint_0^\infty \alpha \bar{P}_{n,m}(\alpha) f_n(\alpha, z) J_m(\alpha r_n) d\alpha, \quad (22)$$

where the integral is interpreted as

$$\oint_0^\infty \frac{s(x)}{x - x_0} dx = \int_0^\infty \frac{s(x)}{x - x_0} dx + \pi i s(x_0), \quad (23)$$

so that the radiation condition requiring diffracted waves propagating outwards is satisfied [19], see details in Appendix A.

The diffracted potential is ultimately expressed in terms of  $\bar{P}_{n,m}$  as

$$\begin{aligned}\phi_D &= \sum_{n=1}^N \sum_{m=-\infty}^{\infty} \phi_{n,m}(r_n, z) e^{im\theta_n} = \sum_{m=-\infty}^{\infty} \phi_{n,m}(r_n, z) e^{im\theta_n} + \sum_{\substack{j=1 \\ j \neq n}}^N \sum_{m=-\infty}^{\infty} \phi_{j,m}(r_j, z) e^{im\theta_j} \\ &= \sum_{m=-\infty}^{\infty} e^{im\theta_n} \int_0^{\infty} \alpha \bar{P}_{n,m}(\alpha) f_n(\alpha, z) J_m(\alpha r_n) d\alpha \\ &\quad + \sum_{\substack{j=1 \\ j \neq n}}^N \sum_{m=-\infty}^{\infty} \int_0^{\infty} \alpha \bar{P}_{j,m}(\alpha) f_j(\alpha, z) \sum_{m'=-\infty}^{\infty} J_{m-m'}(\alpha R_{j,n}) e^{i(m-m')\alpha_{j,n}} J_{m'}(\alpha r_n) e^{im'\theta_n} d\alpha.\end{aligned}\tag{24}$$

Note that Graf's addition theorem for Bessel functions [26]

$$J_m(kr_j) e^{im\theta_j} = \sum_{m'=-\infty}^{\infty} J_{m-m'}(kR_{j,n}) e^{i(m-m')\alpha_{j,n}} J_{m'}(kr_n) e^{im'\theta_n},\tag{25}$$

has been adopted in Eq. (24);  $R_{j,n}$  and  $\alpha_{j,n}$  represent the module and the angle, respectively, of  $\overrightarrow{O_j O_n}$ . It should be pointed out that Eq. (25) has no geometric restrictions in its use in contrast to the application of Graf's addition theorem to Hankel functions which is required in other approaches involved in circular scattering problems [e.g., see 11, 12, 27]. Therefore, the present model is available for arbitrary distributions of the plates, including the staggered arrangement. For the particular case when the plates are coaxial, i.e.,  $R_{j,n} = 0$ , Eq. (25) reduces to  $J_m(kr_j) e^{im\theta_j} = J_m(kr_n) e^{im\theta_n}$ , i.e., no transform is required as expected, and for this particular case, the final expression of  $\phi_D$ , i.e., Eq. (24), can be further simplified.

### III. NUMERICAL METHOD

The Galerkin method can be employed to solve the hydrodynamic problem. In the linearized hydrodynamic model, the fluid velocity and the hydrodynamic pressure are square-root singular at the edge of a thin plate. To incorporate the known null velocity potential jump and the square-root behavior of velocity at the edge of the plate,  $P_{n,m}$  may be expressed as [e.g., see 16, 17]

$$P_{n,m}(r_n) = \sum_{q=0}^{\infty} \alpha_{m,q}^{(n)} \Phi_q^{(|m|)} \left( \frac{r_n}{R_n} \right),\tag{26}$$

in which  $\alpha_q^{n,m}$  are the unknown coefficients to be determined, and

$$\Phi_q^{(m)}(x) = \frac{q! \Gamma(m + (1/2))}{\sqrt{2\pi} \Gamma(q + m + (3/2))} x^m C_{2q+1}^{m+1/2}(\sqrt{1-x^2}),\tag{27}$$

where  $C_{2q+1}^{m+1/2}$  is the Gegenbauer polynomial and  $\Gamma$  the Gamma function. It is noted that the functions  $\Phi_q^{(m)}(x)$  incorporate the correct square-root behavior at  $x = 1$ , and it has the orthogonal property [e.g., see 26], satisfying

$$\int_0^1 \Phi_q^{(|m|)}(x) \Phi_l^{(|m|)}(x) \frac{x}{\sqrt{1-x^2}} dx = \begin{cases} 0, & q \neq l, \\ \frac{(2|m|+2q+1)!(q!)^2}{4^{|m|+1}(2q+1)! (|m|+2q+\frac{3}{2}) [\Gamma(|m|+q+\frac{3}{2})]^2}, & q = l. \end{cases} \quad (28)$$

By applying the identity [e.g., see 16]

$$\int_0^1 \Phi_q^{(|m|)}(x) J_m(\xi x) x dx = \mu_m \frac{J_{|m|+2q+3/2}(\xi)}{\xi^{3/2}}, \quad (29)$$

where  $\mu_m = 1$  and  $(-1)^m$  for  $m \geq 0$  and  $m < 0$ , respectively, we obtain

$$\bar{P}_{n,m}(\alpha) = \int_0^{R_n} r_n P_{n,m}(r_n) J_m(\alpha r_n) dr_n = R_n^2 \sum_{q=0}^{\infty} \alpha_{m,q}^{(n)} \mu_m \frac{J_{|m|+2q+3/2}(\alpha R_n)}{(\alpha R_n)^{3/2}}. \quad (30)$$

### A. Rigid circular plates

For fixed rigid circular plates, we have  $\eta_n = 0$  in Eq. (9). After multiplying each side of Eq. (9) by  $e^{-i\tau\theta_n} \Phi_{\zeta}^{(|\tau|)}\left(\frac{r_n}{R_n}\right) r_n$  and integrating over  $\theta_n \in [0, 2\pi]$  and  $r_n \in [0, R_n]$ , and making some rearrangements, we have

$$\begin{aligned} & \frac{1}{R_n} \sum_{q=0}^{\infty} \alpha_{\tau,q}^{(n)} \int_0^{\infty} F_{n,n,q}^{\tau,\tau,\zeta}(\alpha) d\alpha \\ & + \sum_{\substack{j=1 \\ j \neq n}}^N \sum_{m=-\infty}^{\infty} \mu_{\tau} \mu_m e^{i(m-\tau)\alpha_{j,n}} \frac{R_j^{1/2}}{R_n^{3/2}} \sum_{q=0}^{\infty} \alpha_{m,q}^{(j)} \int_0^{\infty} F_{n,j,q}^{m,\tau,\zeta}(\alpha) J_{m-\tau}(\alpha R_{j,n}) d\alpha \\ & + i p_n \sum_{q=0}^{\infty} \alpha_{\tau,q}^{(n)} \frac{q! \zeta! [\Gamma(|\tau| + \frac{1}{2})]^2}{2\pi \Gamma(q + |\tau| + \frac{3}{2}) \Gamma(\zeta + |\tau| + \frac{3}{2})} \int_0^1 C_{2q+1}^{|\tau|+\frac{1}{2}}(x) C_{2\zeta+1}^{|\tau|+\frac{1}{2}}(x) (1-x^2)^{|\tau|} x dx \\ & = \frac{igA}{\omega} Z'(-d_n) \mu_{\tau} i^{\tau} e^{-i\tau\beta} e^{ik(x_n \cos\beta + y_n \sin\beta)} \frac{J_{|\tau|+2\zeta+3/2}(kR_n)}{(kR_n)^{3/2}}, \end{aligned} \quad (31)$$

where

$$F_{n,j,q}^{m,\tau,\zeta}(\alpha) = \left. \frac{\partial f_j(\alpha, z)}{\partial z} \right|_{z=-d_n} \frac{J_{|\tau|+2\zeta+3/2}(\alpha R_n) J_{|m|+2q+3/2}(\alpha R_j)}{\alpha^2}, \quad (32)$$

in which

$$\left. \frac{\partial f_j(\alpha, z)}{\partial z} \right|_{z=-d_n} = \begin{cases} \frac{\alpha \sinh[\alpha(h-d_j)] [-\alpha \sinh(\alpha d_n) + K \cosh(\alpha d_n)]}{\alpha \sinh(\alpha h) - K \cosh(\alpha h)}, & d_n \leq d_j \\ \frac{\alpha \sinh[\alpha(h-d_n)] [-\alpha \sinh(\alpha d_j) + K \cosh(\alpha d_j)]}{\alpha \sinh(\alpha h) - K \cosh(\alpha h)}, & d_n \geq d_j \end{cases}, \quad (33)$$

and the first and second lines on left-hand side of Eq. (31) involve two semi-infinite integrands with the decays of  $\alpha^{-2}$  and  $e^{-|d_j-d_n|\alpha}\alpha^{-2.5}$ , respectively.

In order to evaluate the unknown coefficients  $\alpha_{m,q}^{(n)}$ , we truncate all infinite series of  $q$  at  $L$ , i.e.,  $(L+1)$  terms ( $q = 0, 1, \dots, L$ ), and we take  $(2M+1)$  angular terms ( $m = -M, \dots, 0, \dots, M$ ), resulting in  $N(2M+1)(L+1)$  unknown coefficients to be determined. After taking  $(\tau = -M, \dots, 0, \dots, M)$  and  $(\zeta = 0, 1, \dots, L)$  in Eq. (33),  $N(2M+1)(L+1)$  equations are obtained, which can be used to determine the exact same number of unknown coefficients.

The case of infinite depth can be treated in a similar manner and leads to exactly the same type of formulation but with

$$f_n(\alpha, z) = \begin{cases} e^{-\alpha d_n} [\alpha \cosh(\alpha z) + K \sinh(\alpha z)], & -d_n \leq z \leq 0 \\ \frac{e^{\alpha z} [\alpha - K]}{e^{\alpha d_n} [-\alpha \sinh(\alpha d_n) + K \cosh(\alpha d_n)]}, & -h < z \leq -d_n \end{cases}, \quad (34)$$

and

$$\left. \frac{\partial f_j(\alpha, z)}{\partial z} \right|_{z=-d_n} = \begin{cases} \frac{\alpha e^{-\alpha d_j} [-\alpha \sinh(\alpha d_n) + K \cosh(\alpha d_n)]}{\alpha - K}, & d_n \leq d_j \\ \frac{\alpha e^{-\alpha d_n} [-\alpha \sinh(\alpha d_j) + K \cosh(\alpha d_j)]}{\alpha - K}, & d_n \geq d_j \end{cases}. \quad (35)$$

The present work is focused on the finite water depth, hence hereinafter the fluid is assumed of finite depth.

## B. Flexible circular plates

For the cases of flexible circular plates, the deformation of the  $n$ th plate  $\eta_n$  excited by water waves can be expressed as [e.g., see 28]

$$\eta_n = \sum_{m=-\infty}^{\infty} \sum_{l=0}^{\infty} \left[ A_{m,l}^{(n)} J_m \left( \mu_{m,l}^{(n)} \frac{r_n}{R_n} \right) + B_{m,l}^{(n)} I_m \left( \mu_{m,l}^{(n)} \frac{r_n}{R_n} \right) \right] e^{im\theta_n}, \quad (36)$$

where  $I_m$  denote the modified Bessel functions of the first kind and  $m$ th order.  $\mu_{m,l}^{(n)} = \mu_{-m,l}^{(n)}$ , and  $\mu_{|m|,l}^{(n)} \in \mathbb{R}^+$  are the eigenvalues of plate free vibration numbered in ascending order of their magnitude.  $A_{m,l}^{(n)}$  and  $B_{m,l}^{(n)}$  are the unknown coefficients to be determined. In the present work, the circular plates are assumed to have either a simply supported or a clamped edge condition, i.e.,  $\eta_n = 0$  should be satisfied at  $r_n = R_n$ , resulting in

$$B_{m,l}^{(n)} = -\frac{J_m(\mu_{m,l}^{(n)})}{I_m(\mu_{m,l}^{(n)})} A_{m,l}^{(n)}. \quad (37)$$

The eigenvalues  $\mu_{m,l}^{(n)}$  depend on both the plate shape and the edge conditions of the plate. In particular, for the circular plates with clamped edges, we have

$$\begin{cases} A_{m,l}^{(n)} J_m(\mu_{m,l}^{(n)}) + B_{m,l}^{(n)} I_m(\mu_{m,l}^{(n)}) = 0, \\ A_{m,l}^{(n)} J'_m(\mu_{m,l}^{(n)}) + B_{m,l}^{(n)} I'_m(\mu_{m,l}^{(n)}) = 0. \end{cases} \quad (38)$$

To have nonzero solutions of  $A_{m,l}^{(n)}$  and  $B_{m,l}^{(n)}$ , the determinant of the coefficient matrix should be equal to 0, and  $\mu_{m,l}^{(n)}$  for  $m \geq 0$  are the roots of

$$J_m(x) I'_m(x) - J'_m(x) I_m(x) = 0, \quad (39)$$

i.e.,

$$J_m(x) I_{m+1}(x) + J_{m+1}(x) I_m(x) = 0. \quad (40)$$

For the simply supported edge conditions [e.g., see 11], we have

$$\begin{cases} A_{m,l}^{(n)} J_m + B_{m,l}^{(n)} I_m = 0, \\ A_{m,l}^{(n)} [(\mu_{m,l}^{(n)})^2 J''_m + \mu_{m,l}^{(n)} \nu J'_m - m^2 \nu J_m] + B_{m,l}^{(n)} [(\mu_{m,l}^{(n)})^2 I''_m + \mu_{m,l}^{(n)} \nu I'_m - m^2 \nu I_m] = 0, \end{cases} \quad (41)$$

where  $\nu$  denotes Poisson ratio.  $\nu = 0.3$  is employed in this paper for the sake of example, and the argument  $\mu_{m,l}^{(n)}$  in Bessel functions has been omitted for brevity.

Therefore, the eigenvalues,  $\mu_{m,l}^{(n)}$  for  $m \geq 0$ , associated with the circular plates with the simply supported edge conditions are the roots of

$$[x^2 I''_m(x) + x \nu I'_m(x) - m^2 \nu I_m(x)] J_m(x) - [x^2 J''_m(x) + x \nu J'_m(x) - m^2 \nu J_m(x)] I_m(x) = 0, \quad (42)$$

i.e.,

$$2x I_m(x) J_m(x) - (1 - \nu) [I_{m+1}(x) J_m(x) + J_{m+1}(x) I_m(x)] = 0. \quad (43)$$

After multiplying each side of Eq. (11) by

$$e^{-i\tau\theta_n} \left[ J_\tau \left( \mu_{\tau,\zeta}^{(n)} \frac{r_n}{R_n} \right) - \frac{J_\tau(\mu_{\tau,\zeta}^{(n)})}{I_\tau(\mu_{\tau,\zeta}^{(n)})} I_\tau \left( \mu_{\tau,\zeta}^{(n)} \frac{r_n}{R_n} \right) \right] r_n,$$

and integrating over  $\theta_n \in [0, 2\pi]$  and  $r_n \in [0, R_n]$ , utilizing the orthogonality of the dry modes of the plates, and making some rearrangements, we have

$$\begin{aligned} & A_{\tau,\zeta}^{(n)} \left[ \left( \mu_{\tau,\zeta}^{(n)} \right)^4 - \frac{\omega^2 R_n^4 \gamma_n}{g \chi_n} \right] \int_0^1 x \left[ J_\tau \left( \mu_{\tau,\zeta}^{(n)} x \right) - \frac{J_\tau(\mu_{\tau,\zeta}^{(n)})}{I_\tau(\mu_{\tau,\zeta}^{(n)})} I_\tau \left( \mu_{\tau,\zeta}^{(n)} x \right) \right]^2 dx \\ & + \frac{i\omega R_n^4}{g \chi_n} \sum_{q=0}^{\infty} \alpha_{\tau,q}^{(n)} \left[ \mu_\tau \frac{J_{|\tau|+2q+3/2}(\mu_{\tau,\zeta}^{(n)})}{(\mu_{\tau,\zeta}^{(n)})^{3/2}} - (-1)^q \frac{J_\tau(\mu_{\tau,\zeta}^{(n)})}{I_\tau(\mu_{\tau,\zeta}^{(n)})} \frac{I_{|\tau|+2q+3/2}(\mu_{\tau,\zeta}^{(n)})}{(\mu_{\tau,\zeta}^{(n)})^{3/2}} \right] = 0, \end{aligned} \quad (44)$$

with which  $A_{\tau,\zeta}^{(n)}$  can be expressed in terms of  $\alpha_{\tau,q}^{(n)}$ .

After multiplying each side of Eq. (9) by  $e^{-i\tau\theta_n}\Phi_{\zeta}^{(|\tau|)}(\frac{r_n}{R_n})r_n$  and integrating over  $\theta_n \in [0, 2\pi]$  and  $r_n \in [0, R_n]$ , and making some rearrangements, we have

$$\begin{aligned}
& \frac{1}{R_n} \sum_{q=0}^{\infty} \alpha_{\tau,q}^{(n)} \int_0^{\infty} F_{n,n,q}^{\tau,\tau,\zeta}(\alpha) d\alpha \\
& + \sum_{\substack{j=1 \\ j \neq n}}^N \sum_{m=-\infty}^{\infty} \mu_{\tau} \mu_m e^{i(m-\tau)\alpha_{j,n}} \frac{R_j^{1/2}}{R_n^{3/2}} \sum_{q=0}^{\infty} \alpha_{m,q}^{(j)} \int_0^{\infty} F_{n,j,q}^{m,\tau,\zeta}(\alpha) J_{m-\tau}(\alpha R_{j,n}) d\alpha \\
& + i p_n \sum_{q=0}^{\infty} \alpha_{\tau,q}^{(n)} \frac{q! \zeta! [\Gamma(|\tau| + \frac{1}{2})]^2}{2\pi \Gamma(q + |\tau| + \frac{3}{2}) \Gamma(\zeta + |\tau| + \frac{3}{2})} \int_0^1 C_{2q+1}^{|\tau|+\frac{1}{2}}(x) C_{2\zeta+1}^{|\tau|+\frac{1}{2}}(x) (1-x^2)^{|\tau|} x dx \quad (45) \\
& + i\omega \sum_{l=0}^{\infty} A_{\tau,l}^{(n)} \left[ \mu_{\tau} \frac{J_{|\tau|+2\zeta+3/2}(\mu_{\tau,l}^{(n)})}{(\mu_{\tau,l}^{(n)})^{3/2}} - (-1)^{\zeta} \frac{J_{\tau}(\mu_{\tau,l}^{(n)})}{I_{\tau}(\mu_{\tau,l}^{(n)})} \frac{I_{|\tau|+2\zeta+3/2}(\mu_{\tau,l}^{(n)})}{(\mu_{\tau,l}^{(n)})^{3/2}} \right] \\
& = \frac{igA}{\omega} Z'(-d_n) \mu_{\tau} i^{\tau} e^{-i\tau\beta} e^{ik(x_n \cos \beta + y_n \sin \beta)} \frac{J_{|\tau|+2\zeta+3/2}(kR_n)}{(kR_n)^{3/2}}.
\end{aligned}$$

After inserting Eq. (44) into Eq. (45) and truncating the series of  $\alpha_{m,q}^{(n)}$ , the unknown coefficients  $\alpha_{m,q}^{(n)}$  can be solved numerically in a similar way as reported in Sec. III A, and  $A_{m,l}^{(n)}$  can then be calculated from Eq. (44).

### C. Free-surface elevation

Once the velocity potential in the fluid domain is predicted, the free-surface elevation  $\mathcal{E}$  can be calculated in a straightforward manner,

$$\begin{aligned}
\mathcal{E} &= \frac{i\omega}{g} \phi|_{z=0} = \frac{i\omega}{g} \left[ \phi_I|_{z=0} + \sum_{n=1}^N \sum_{m=-\infty}^{\infty} \phi_{n,m}(r_n, 0) e^{im\theta_n} \right] \\
&= A e^{ik(x \cos \beta + y \sin \beta)} + \frac{i\omega}{g} \sum_{n=1}^N \sum_{m=-\infty}^{\infty} \left[ \sum_{q=0}^{\infty} \alpha_{m,q}^{(n)} \int_0^{\infty} J_{|m|+2q+3/2}(\alpha R_n) \right. \\
&\quad \times \left. \frac{(\alpha R_n)^{1/2} \sinh[\alpha(h-d_n)]}{\alpha \sinh(\alpha h) - K \cosh(\alpha h)} J_{|m|}(\alpha r_n) d\alpha \right] e^{im\theta_n}. \quad (46)
\end{aligned}$$



#### D. Velocity vector of the fluid

The components of the velocity vector  $\vec{u} = (u_x, u_y, u_z)$  may be expressed as

$$\begin{aligned}
 u_x &= \frac{\partial \phi}{\partial x} = \frac{\partial \phi_I}{\partial x} + \sum_{n=1}^N \sum_{m=-\infty}^{\infty} \left[ \frac{\partial \phi_{n,m}(r_n, z)}{\partial r_n} \cos \theta_n - i m r_n \phi_{n,m}(r_n, z) \sin \theta_n \right] e^{im\theta_n} \\
 &= \frac{gkA \cos \beta}{\omega} Z(z) e^{ik(x \cos \beta + y \sin \beta)} + \sum_{n=1}^N \sum_{m=-\infty}^{\infty} \left[ \sum_{q=0}^{\infty} \alpha_{m,q}^{(n)} \int_0^{\infty} J_{|m|+2q+3/2}(\alpha R_n) \right. \\
 &\quad \times \left. \frac{(R_n)^{1/2} f_n(\alpha, z)}{\alpha^{1/2}} (\alpha J'_{|m|}(\alpha r_n) \cos \theta_n - i m r_n J_{|m|}(\alpha r_n) \sin \theta_n) d\alpha \right] e^{im\theta_n},
 \end{aligned} \tag{47}$$

$$\begin{aligned}
 u_y &= \frac{\partial \phi}{\partial y} = \frac{\partial \phi_I}{\partial y} + \sum_{n=1}^N \sum_{m=-\infty}^{\infty} \left[ \frac{\partial \phi_{n,m}(r_n, z)}{\partial r_n} \sin \theta_n + i m r_n \phi_{n,m}(r_n, z) \cos \theta_n \right] e^{im\theta_n} \\
 &= \frac{gkA \sin \beta}{\omega} Z(z) e^{ik(x \cos \beta + y \sin \beta)} + \sum_{n=1}^N \sum_{m=-\infty}^{\infty} \left[ \sum_{q=0}^{\infty} \alpha_{m,q}^{(n)} \int_0^{\infty} J_{|m|+2q+3/2}(\alpha R_n) \right. \\
 &\quad \times \left. \frac{(R_n)^{1/2} f_n(\alpha, z)}{\alpha^{1/2}} (\alpha J'_{|m|}(\alpha r_n) \sin \theta_n + i m r_n J_{|m|}(\alpha r_n) \cos \theta_n) d\alpha \right] e^{im\theta_n},
 \end{aligned} \tag{48}$$

and

$$\begin{aligned}
 u_z &= \frac{\partial \phi}{\partial z} = \frac{\partial \phi_I}{\partial z} + \sum_{n=1}^N \sum_{m=-\infty}^{\infty} \frac{\partial \phi_{n,m}(r_n, z)}{\partial z} e^{im\theta_n} \\
 &= \frac{-igA}{\omega} Z'(z) e^{ik(x \cos \beta + y \sin \beta)} + \sum_{n=1}^N \sum_{m=-\infty}^{\infty} \left[ \sum_{q=0}^{\infty} \alpha_{m,q}^{(n)} \int_0^{\infty} J_{|m|+2q+3/2}(\alpha R_n) \right. \\
 &\quad \times \left. \frac{(R_n)^{1/2}}{\alpha^{1/2}} \frac{\partial f_n(\alpha, z)}{\partial z} J_{|m|}(\alpha r_n) d\alpha \right] e^{im\theta_n},
 \end{aligned} \tag{49}$$

respectively.

#### E. Strain on the plate

The strain of the plate could be an important physical parameter to predict the fracture and breakup of the plate. The strain tensor matrix of the  $n$ th plate can be written as [29, 30]

$$\boldsymbol{\epsilon}_n = \frac{h^2}{A} \begin{bmatrix} \epsilon_{r_n r_n}^{(n)} & \epsilon_{r_n \theta_n}^{(n)} \\ \epsilon_{r_n \theta_n}^{(n)} & \epsilon_{\theta_n \theta_n}^{(n)} \end{bmatrix} = \frac{h^2}{A} \begin{bmatrix} \frac{\partial^2 W_n}{\partial r_n^2} & \frac{\partial^2 W_n}{r_n \partial r_n \partial \theta_n} - \frac{\partial W_n}{r_n^2 \partial \theta_n} \\ \frac{\partial^2 W_n}{r_n \partial r_n \partial \theta_n} - \frac{\partial W_n}{r_n^2 \partial \theta_n} & \frac{\partial W_n}{r_n \partial r_n} + \frac{\partial^2 W_n}{r_n^2 \partial \theta_n^2} \end{bmatrix}, \tag{50}$$

where  $W_n = \text{Re}\{\eta_n e^{-i\omega t}\}$ .

The eigenvalues  $\varsigma_1^{(n)}$  and  $\varsigma_2^{(n)}$  of the strain tensor matrix  $\boldsymbol{\epsilon}_n$  can be obtained as

$$\begin{aligned} \varsigma_{1,2}^{(n)} = \frac{h^2}{2A} \left\{ \left( \frac{\partial^2 W_n}{\partial r_n^2} + \frac{\partial W_n}{r_n \partial r_n} + \frac{\partial^2 W_n}{r_n^2 \partial \theta_n^2} \right) \right. \\ \left. \pm \left[ \left( \frac{\partial^2 W_n}{\partial r_n^2} - \frac{\partial W_n}{r_n \partial r_n} - \frac{\partial^2 W_n}{r_n^2 \partial \theta_n^2} \right)^2 + 4 \left( \frac{\partial^2 W_n}{r_n \partial r_n \partial \theta_n} - \frac{\partial W_n}{r_n^2 \partial \theta_n} \right)^2 \right]^{1/2} \right\}. \end{aligned} \quad (51)$$

The maximum principal strain  $\epsilon_{max}^{(n)}$  at a given location may be then determined as the maximum value of  $|\varsigma_{1,2}^{(n)}|$  as  $t$  varies from 0 to  $2\pi/\omega$  [30].

## F. Wave excitation forces

The wave excitation forces acting on each plate can be calculated by integrating the velocity potential jump over the plate area.

The heave excitation force on the  $n$ th plate is given by

$$F_3^{(n)} = -i\omega\rho \int_0^{2\pi} \int_0^{R_n} P_n(r_n, \theta_n) r_n dr_n d\theta_n = -\frac{2}{3}i\omega\rho \sqrt{2\pi} R_n^2 \alpha_{0,0}^{(n)}, \quad (52)$$

where

$$\Phi_0^{(0)}(x) = \frac{\Gamma(1/2)}{\sqrt{2\pi}\Gamma(3/2)} C_1^{1/2}(\sqrt{1-x^2}) = \sqrt{2/\pi} \sqrt{1-x^2}, \quad (53)$$

together with the orthogonal property given in Eq. (28), is applied.

The roll excitation moment on the  $n$ th plate is given by

$$F_4^{(n)} = -i\omega\rho \int_0^{2\pi} \int_0^{R_n} P_n(r_n, \theta_n) (r_n \sin \theta_n) r_n dr_n d\theta_n = \frac{2}{15}\omega\rho \sqrt{2\pi} R_n^3 (\alpha_{1,0}^{(n)} - \alpha_{-1,0}^{(n)}), \quad (54)$$

in which

$$\Phi_0^{(1)}(x) = \frac{\Gamma(3/2)}{\sqrt{2\pi}\Gamma(5/2)} C_1^{3/2}(\sqrt{1-x^2}) = \sqrt{2/\pi} x \sqrt{1-x^2}, \quad (55)$$

together with the orthogonal property given in Eq. (28), is utilized.

The pitch excitation moment on the  $n$ th plate is given by

$$F_5^{(n)} = i\omega\rho \int_0^{2\pi} \int_0^{R_n} P_n(r_n, \theta_n) (r_n \cos \theta_n) r_n dr_n d\theta_n = \frac{2}{15}i\omega\rho \sqrt{2\pi} R_n^3 (\alpha_{1,0}^{(n)} + \alpha_{-1,0}^{(n)}). \quad (56)$$

## G. Wave power dissipation

Due to the resistance effect of the porosity, wave power can be dissipated by the array of perforated plates.

### 1. Direct method

The time-averaged energy dissipated by the plates  $P_{diss}$  can be calculated in a straightforward manner by integrating the power dissipated per unit area over the plates

$$\begin{aligned}
P_{diss} &= \frac{\rho\omega}{2} \sum_{n=1}^N \text{Re}(p_n) \int_0^{R_n} \int_0^{2\pi} |\phi_n^+ - \phi_n^-|^2 r_n dr_n d\theta_n \\
&= \frac{\rho\omega}{2} \sum_{n=1}^N \text{Re}(p_n) R_n^2 \sum_{m=-\infty}^{\infty} \sum_{q=0}^{\infty} \sum_{\zeta=0}^{\infty} \alpha_{m,q}^{(n)} \alpha_{m,\zeta}^{(n)*} \frac{q! \zeta! [\Gamma(|m| + (1/2))]^2}{\Gamma(q + |m| + (3/2)) \Gamma(\zeta + |m| + (3/2))} \\
&\quad \times \int_0^1 (1-x^2)^{|m|} C_{2q+1}^{|m|+1/2}(x) C_{2\zeta+1}^{|m|+1/2}(x) x dx.
\end{aligned} \tag{57}$$

The wave power dissipation can be further nondimensionalized as

$$\kappa_{diss} = \frac{k P_{diss}}{P_{in}}, \tag{58}$$

in which  $P_{in}$  denotes the incoming wave power per unit width of the wave front

$$P_{in} = \frac{\rho g A^2 \omega}{2} \frac{1}{2k} \left[ 1 + \frac{2kh}{\sinh(2kh)} \right]. \tag{59}$$

### 2. Indirect method

For  $kr_n \rightarrow \infty$ , we find,

$$\phi_{n,m}(r_n, z) \sim A_{n,m} H_m(kr_n) Z(z), \tag{60}$$

where  $H_m = J_m + iY_m$  represents the first kind Hankel functions of the  $m$ th order, and

$$\begin{aligned}
A_{n,m} &= \frac{i\pi k \sinh[k(h - d_n)] \cosh(kh) \bar{P}_{n,m}(k)}{2hN_0} \\
&= \frac{i\pi k \sinh[k(h - d_n)] \cosh(kh)}{2hN_0} R_n^2 \sum_{q=0}^{\infty} \alpha_{m,q}^{(n)} \mu_m \frac{J_{|m|+2q+3/2}(kR_n)}{(kR_n)^{3/2}}.
\end{aligned} \tag{61}$$

Following [11], the time-averaged power dissipated by the array of plates can be expressed indirectly in terms of the Kochin functions [e.g., see 31],

$$P_{diss} = \frac{\rho\omega D(kh)}{k} \left\{ \frac{Ag}{2\omega} \text{Re}[H_R(\beta)] - \frac{1}{8\pi} \int_0^{2\pi} |H_R(\theta_0)|^2 d\theta_0 \right\}, \tag{62}$$

where

$$D(kh) = \left[ 1 + \frac{2kh}{\sinh(2kh)} \right] \tanh(kh), \tag{63}$$

and  $H_R$  is the Kochin function, which can be expressed in terms of  $A_{n,m}$  or  $\alpha_{m,q}^{(n)}$

$$\begin{aligned}
H_R(\theta_0) &= 2 \sum_{n=1}^N \sum_{m=-\infty}^{\infty} A_{n,m} e^{-ikR_{0,n} \cos(\alpha_{0,n} - \theta_0)} (-i)^{m+1} e^{im\theta_0} \\
&= \frac{\pi \cosh(kh)}{khN_0} \sum_{n=1}^N \sum_{m=-\infty}^{\infty} (-i)^m e^{-ikR_{0,n} \cos(\alpha_{0,n} - \theta_0)} e^{im\theta_0} \sinh[k(h - d_n)] (kR_n)^{1/2} \\
&\quad \times \sum_{q=0}^{\infty} \alpha_{m,q}^{(n)} \mu_m J_{|m|+2q+3/2}(kR_n).
\end{aligned} \tag{64}$$

Another way to derive the expression of the wave power dissipation in terms of  $A_{n,m}$  or  $\alpha_{m,q}^{(n)}$ , i.e., Eq. (64), is to separate the propagating modes of the velocity potential at the far-field into incoming waves and outgoing waves, the difference of the power of which is the power lost to the plates. Readers can refer to [32] for a detailed derivation.

#### IV. CONVERGENCE ANALYSIS AND MODEL VALIDATION

The validation of the developed model is now considered. Prior to carrying out any case studies, a convergence analysis should be applied to ensure the results are converged. Figures 3 and 4 illustrate the impact of the angular and radial truncated cutoffs (i.e., in terms of  $M$  and  $L$ ), respectively, on the wave excitation forces/moments acting on a pair of submerged rigid and impermeable circular plates in a staggered arrangement. In order to obtain the converged results,  $M > 8$  and  $L > 4$  are suggested. In this paper,  $M = 10$  and  $L = 6$  are adopted in order to obtain the converged results.

Figure 5 presents the frequency response of the wave excitation forces acting on a pair of submerged rigid and impermeable circular plates in a staggered arrangement. The present semi-analytical results are found to agree well with the numerical ones [33], which are predicted by solving a hypersingular integral equation.

Figures 6 and 7 compare the present semi-analytical results of the contours of the deflection of a single submerged elastic perforated circular plate with simply supported edge conditions and the corresponding wave amplitude above it with the published data by using eigenfunction matching method [12]. Again, an excellent agreement between them is observed.

The examined cases all demonstrate that the present Hankel transform-based model works well in solving water wave interaction with an array of submerged circular plates.

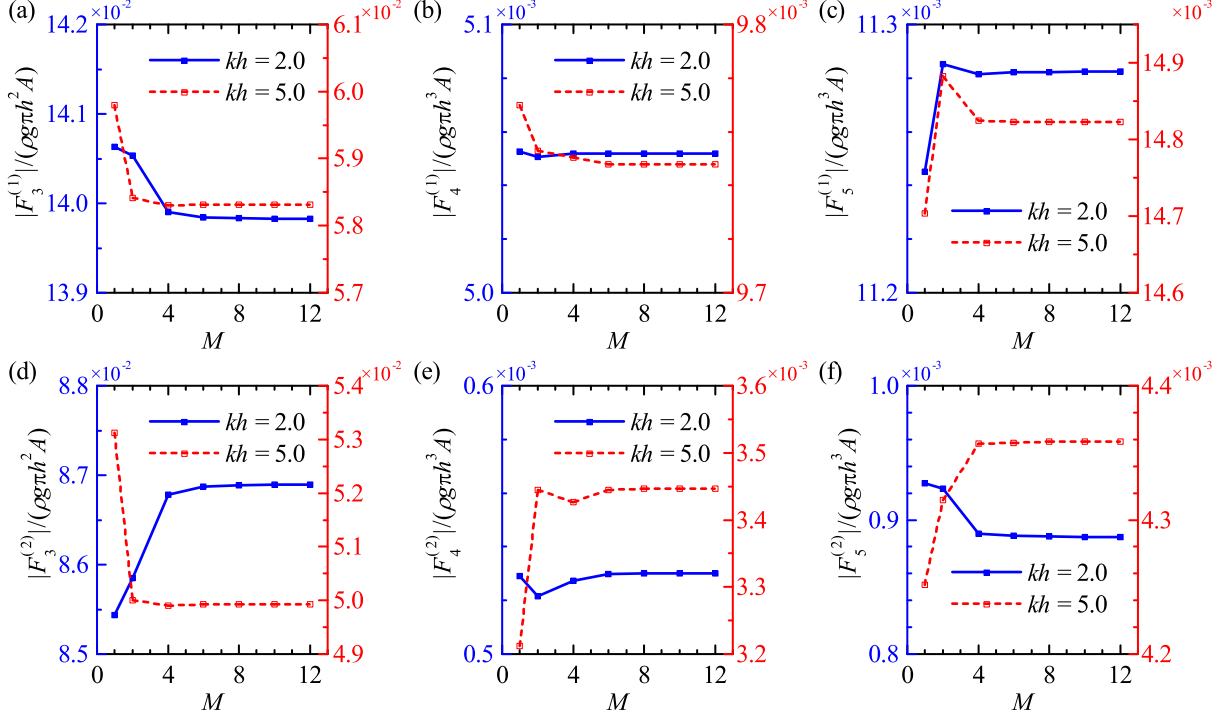


FIG. 3: Impact of the angular cut-offs (i.e., in terms of  $M$ ) on dimensionless wave excitation force/moment acting on a pair of submerged rigid and impermeable circular plates in a staggered arrangement for  $L = 6$ ,  $R_1/h = 0.5$ ,  $d_1/h = 0.2$ ,  $R_2/h = 0.3$ ,  $d_2/h = 0.1$ ,  $x_1 = y_1 = y_2 = 0$ ,  $x_2/h = 0.5$ ,  $\beta = \pi/6$ ,  $kh = 2.0$  and  $5.0$ : (a) and (d) heave excitation forces; (b) and (e) roll excitation moments; (c) and (f) pitch excitation moments. (a)-(c) plate 1; (d)-(f) plate 2.

## V. RESULTS AND DISCUSSIONS

The present model can be employed to study wave interaction with an array of any number of submerged circular plates, i.e.,  $N = 1, 2, 3 \dots$ . Nevertheless, in this section, the validated model is applied to run a series of case studies on the performance of a pair of identical submerged elastic perforated circular plates ( $N = 2$ ). For the sake of simplification,  $R_n = R$ ,  $p_n = p$ ,  $\chi_n = \chi$ , and  $\gamma_n = \gamma$  are employed hereinafter.  $p$ ,  $\chi$ , and  $\gamma$  can be nondimensionalized as  $\bar{p} = ph$ ,  $\bar{\chi} = \chi/h^4$ , and  $\bar{\gamma} = \gamma/h$ , respectively. One of the two plates is placed in a shallow position below the mean water level, i.e.,  $d_1/h = 0.1$ , whereas the other is placed at a deeper position with  $d_2/h = 0.2$ . In the examined cases, the radii, the flexural rigidity, and the mass per unit area of the plates are fixed with  $R/h = 2.0$  and  $\bar{\chi} = \bar{\gamma} = 0.01$ .

The performance of the pair of plates depends on the distance between them ( $R_{1,2} = x_2 - x_1$ ), the incident wave direction ( $\beta$ ), the porosity parameter ( $\bar{p}$ ), and wave number ( $kh$ ). The

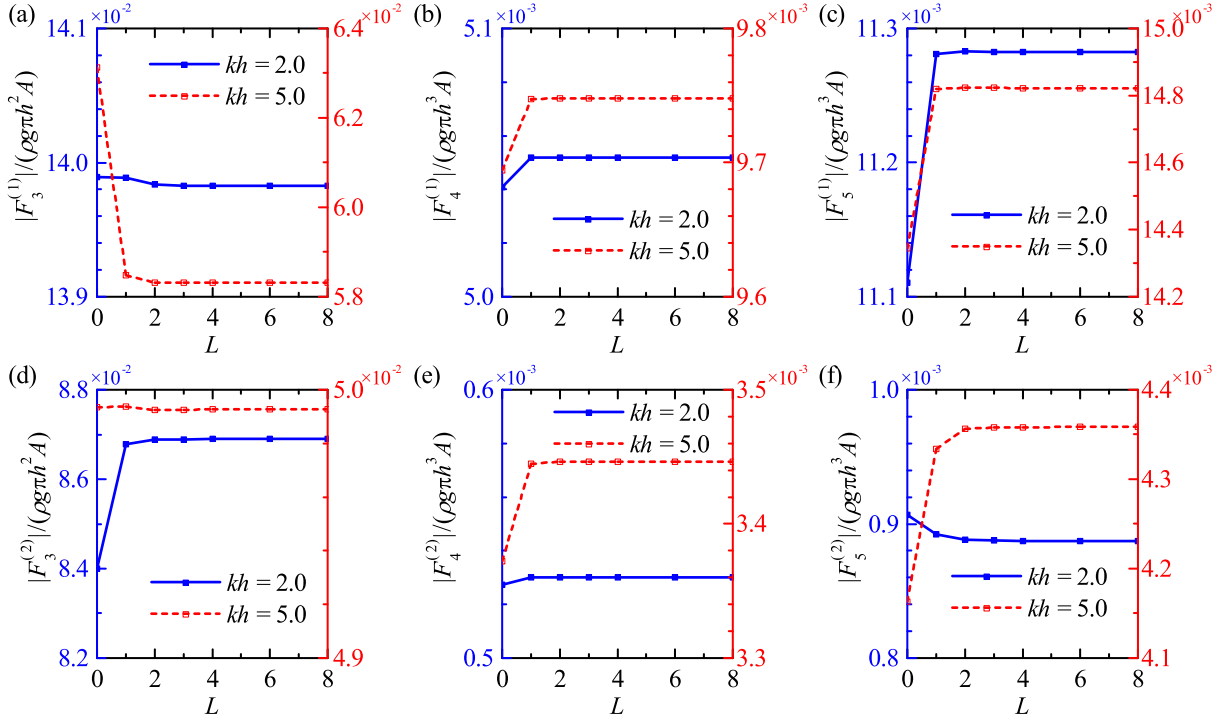


FIG. 4: Impact of the radial cut-offs (i.e., in terms of  $L$ ) on dimensionless wave excitation force/moment acting on a pair of submerged rigid and impermeable circular plates in a staggered arrangement for  $M = 10$ ,  $R_1/h = 0.5$ ,  $d_1/h = 0.2$ ,  $R_2/h = 0.3$ ,  $d_2/h = 0.1$ ,  $x_1 = y_1 = y_2 = 0$ ,  $x_2/h = 0.5$ ,  $\beta = \pi/6$ ,  $kh = 2.0$  and  $5.0$ : (a) and (d) heave excitation forces; (b) and (e) roll excitation moments; (c) and (f) pitch excitation moments. (a)-(c) plate 1; (d)-(f) plate 2.

present Hankel transform-based model enables us to study the performance of the pair of circular plates with any values of  $R_{1,2}$ . Hereinafter, the cases with  $0 \leq R_{1,2}/h \leq 8$  are examined, in which  $R_{1,2}/h = 0$  denotes the coaxial arrangement,  $0 < R_{1,2}/h < 4$  represent the staggered arrangements, whereas  $R_{1,2}/h > 4$  denote the side by side arrangements.

Figure 8 presents the contours of the wave power dissipation ( $\kappa_{diss}$ ) and heave excitation forces ( $|F_3^{(j)}|/(\rho g \pi h^2 A)$  for  $j = 1$  and  $2$ ) acting on the plates with the incident wave direction ( $\beta$ ) ranging from  $0$  to  $\pi$  and the distance between the two plates ( $R_{1,2}/h$ ) for  $\bar{p} = 1.0$  and  $kh = \pi/2$ . For any specific arrangement subjected to a certain wave incident wave direction, the plates with clamped edge conditions are found to dissipate much more wave power compared to those with simply supported edge conditions. Similar results were also reported for a single submerged elastic perforated circular plate [12]. The maximum wave power dissipation can be achieved by the side by side arrangement ( $R_{1,2}/h > 4$ ) with incident waves propagating roughly perpendicular to the

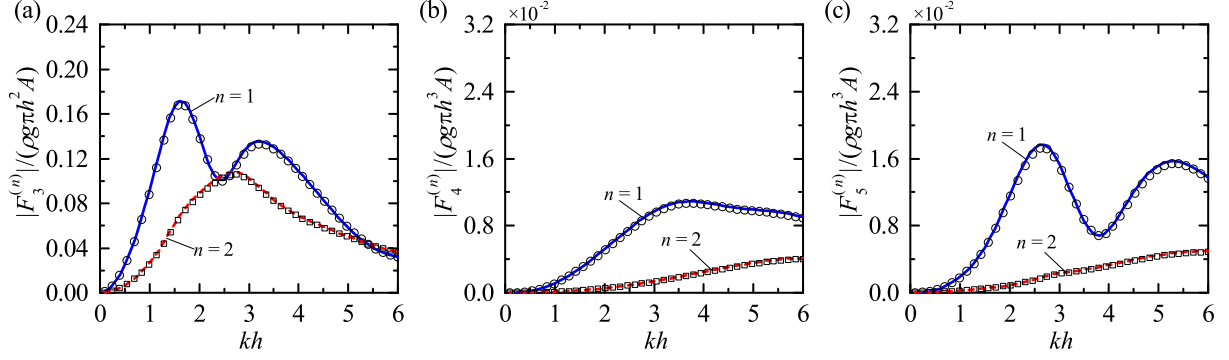


FIG. 5: Variation of dimensionless wave excitation force/moment acting on a pair of submerged rigid and impermeable circular plates in a staggered arrangement vs wave number in terms of  $kh$  for  $R_1/h = 0.5$ ,  $d_1/h = 0.2$ ,  $R_2/h = 0.3$ ,  $d_2/h = 0.1$ ,  $x_1 = y_1 = y_2 = 0$ ,  $x_2/h = 0.5$  and  $\beta = \pi/6$ :

(a) heave excitation forces; (b) roll excitation moments; (c) pitch excitation moments. lines: numerical results [33]; symbols: present semi-analytical results.

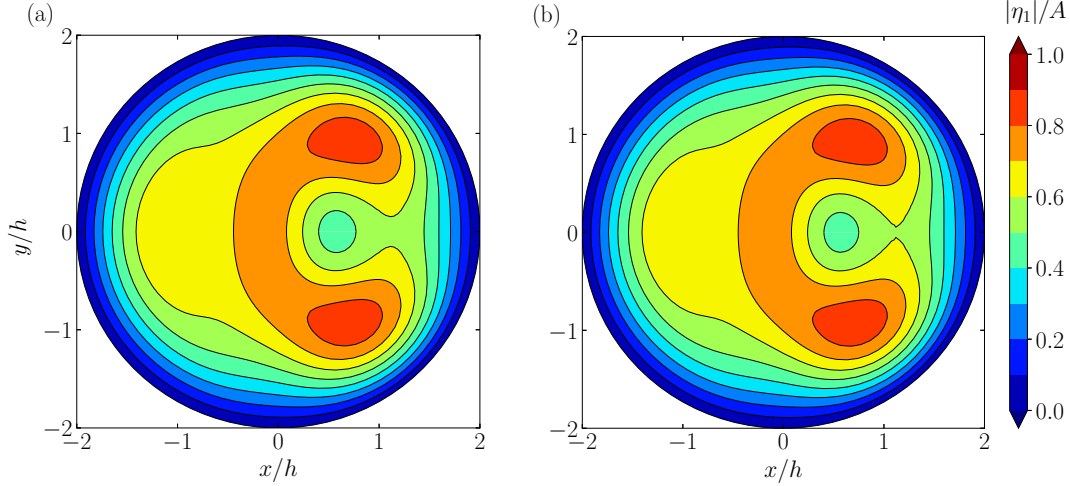


FIG. 6: Contour of the deflection of a single submerged elastic perforated circular plate  $|\eta_1|/A$  for  $R_1/h = 2.0$ ,  $d_1/h = 0.2$ ,  $\bar{\chi} = \bar{\gamma} = 0.01$ ,  $\bar{p} = 1.0$ ,  $\beta = 0$ ,  $kh = \pi/2$  and simply supported edge conditions: (a) published result based on the eigenfunction matching method [12]; (b) present semi-analytical result.

deployment line of the two plates ( $0.2\pi < \beta < 0.7\pi$ ). As the distance between the plates becomes smaller, i.e., the arrangement changes from side by side into staggered or even coaxial, or/and the incident waves propagating at a smaller angle relative to the deployment line of the plates, a dramatic drop of  $\kappa_{diss}$  is observed, particularly for the cases with the clamped edge conditions. The smallest heave excitation forces acting on the two plates with clamped edge conditions both occur

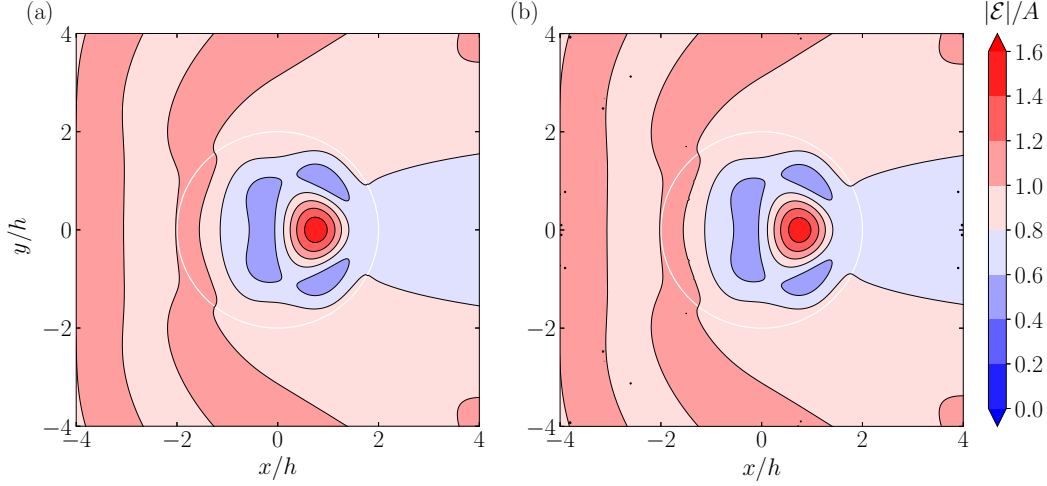


FIG. 7: Contour of the wave amplitude above a single submerged elastic perforated circular plate  $|\mathcal{E}|/A$  for  $R_1/h = 2.0$ ,  $d_1/h = 0.2$ ,  $\bar{\chi} = \bar{\gamma} = 0.01$ ,  $\bar{p} = 1.0$ ,  $\beta = 0$ ,  $kh = \pi/2$  and simply supported edge conditions: (a) published result based on the eigenfunction matching method [12]; (b) present semi-analytical result.

for the staggered arrangement with  $1 < R_{1,2}/h < 2$ , for which the heave excitation forces are even smaller than those for the cases with simply supported edge conditions. For  $R_{1,2}/h < 3$ , the heave excitation forces, especially for the clamped edge cases, are insensitive to the change of incident wave direction. For the side by side arrangement ( $R_{1,2}/h > 4$ ) with the clamped edge conditions, a fluctuation change of the heave wave excitation forces is observed with the change of  $R_{1,2}$  and  $\beta$ , except for  $|F_3^{(1)}|/(\rho g \pi h^2 A)$  around  $\beta = \pi$  and  $|F_3^{(2)}|/(\rho g \pi h^2 A)$  around  $\beta = 0$ , respectively, i.e., the heave wave excitation forces acting on the leeward side plate, which are rather small due to the shadowing effect of the weatherside plate and are insensitive to the change of plate distance in the computed range of  $R_{1,2}$ .

In Fig. 9, the contours of  $\kappa_{diss}$  and  $|F_3^{(j)}|/(\rho g \pi h^2 A)$  for  $j = 1$  and  $2$  with  $\bar{p}$  ranging from 0 to 4 and  $R_{1,2}/h$  are plotted for  $\beta = \pi/2$  and  $kh = \pi/2$ . For any specified arrangement, as  $\bar{p}$  increases from 0 to 4,  $\kappa_{diss}$  first increases and then decreases after reaching the maximum around  $\bar{p} = 0.6$ . Similarly, for any specified porosity parameter  $\bar{p}$ , in the computed range of  $R_{1,2}$ , as  $R_{1,2}/h$  increases from 0 towards 8,  $\kappa_{diss}$  generally increases first and then decreases after reaching the maximum around  $R_{1,2}/h = 6$ . The peak values of  $\kappa_{diss}$  are 7.02 and 10.2 for the simply supported and clamped edge conditions, respectively, both happening at  $(\bar{p}, R_{1,2}/h) = (0.6, 6.0)$ . For  $\bar{p} < 1$ , the heave excitation force acting on the plate, which is located at a shallower position, is found to



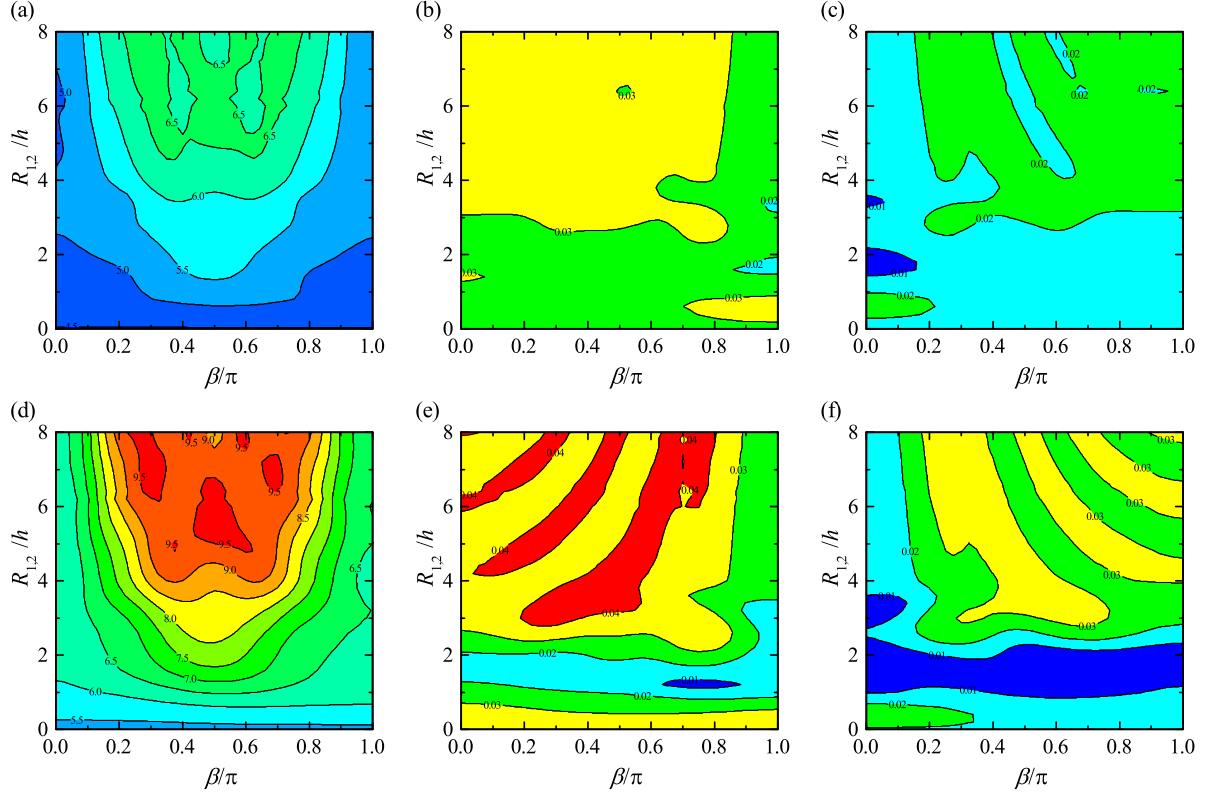


FIG. 8: Contours of wave power dissipation,  $\kappa_{diss}$  ((a) and (d)), heave excitation forces acting on plate 1,  $|F_3^{(1)}|/(\rho g \pi h^2 A)$  ((b) and (e)) and 2,  $|F_3^{(2)}|/(\rho g \pi h^2 A)$  ((c) and (f)) with the incident direction  $\beta$  and the distance between the two plates  $R_{1,2} = x_2 - x_1$  for  $y_1 = y_2 = 0$ ,  $R/h = 2.0$ ,  $d_1/h = 0.1$ ,  $d_2/h = 0.2$ ,  $\bar{\chi} = \bar{\gamma} = 0.01$ ,  $\bar{p} = 1.0$  and  $kh = \pi/2$ : (a)-(c) simply supported edge conditions; (d)-(f) clamped edge conditions.

significantly decrease with the increase of  $\bar{p}$  regardless of the edge conditions.  $|F_3^{(1)}|/(\rho g \pi h^2 A)$  for  $\bar{p} > 1.5$  and  $|F_3^{(2)}|/(\rho g \pi h^2 A)$  for all the computed range of  $\bar{p}$  are rather small.

Figure 10 illustrates the contours of  $\kappa_{diss}$  and  $|F_3^{(j)}|/(\rho g \pi h^2 A)$  for  $j = 1$  and 2 with  $kh$  ranging from  $0.01\pi$  to  $1.0\pi$  and  $R_{1,2}/h$  for  $\beta = \pi/2$  and  $\bar{p} = 1.0$ . As  $kh \rightarrow 0$ ,  $\kappa_{diss}$  and  $|F_3^{(j)}|/(\rho g \pi h^2 A)$  for  $j = 1$  and 2 both vanish regardless of the edge conditions or the values of  $R_{1,2}$  as expected. For any specified arrangement,  $\kappa_{diss}$  increases monotonically with increasing  $kh$ . In the computed range of  $R_{1,2}$ , the side by side arrangements dissipate more wave power than the staggered and coaxial ones. As  $kh$  increases from  $0.01\pi$  to  $0.5\pi$ , an obvious fluctuation change of  $|F_3^{(j)}|/(\rho g \pi h^2 A)$  for  $j = 1$  and 2 is observed with the peaks occurring around  $kh = 0.23\pi$  and  $0.28\pi$  for the simply supported and clamped edge conditions, respectively. This could be explained from the perspective of resonance. The more strictly the circular plates are constrained at their edges, the larger the

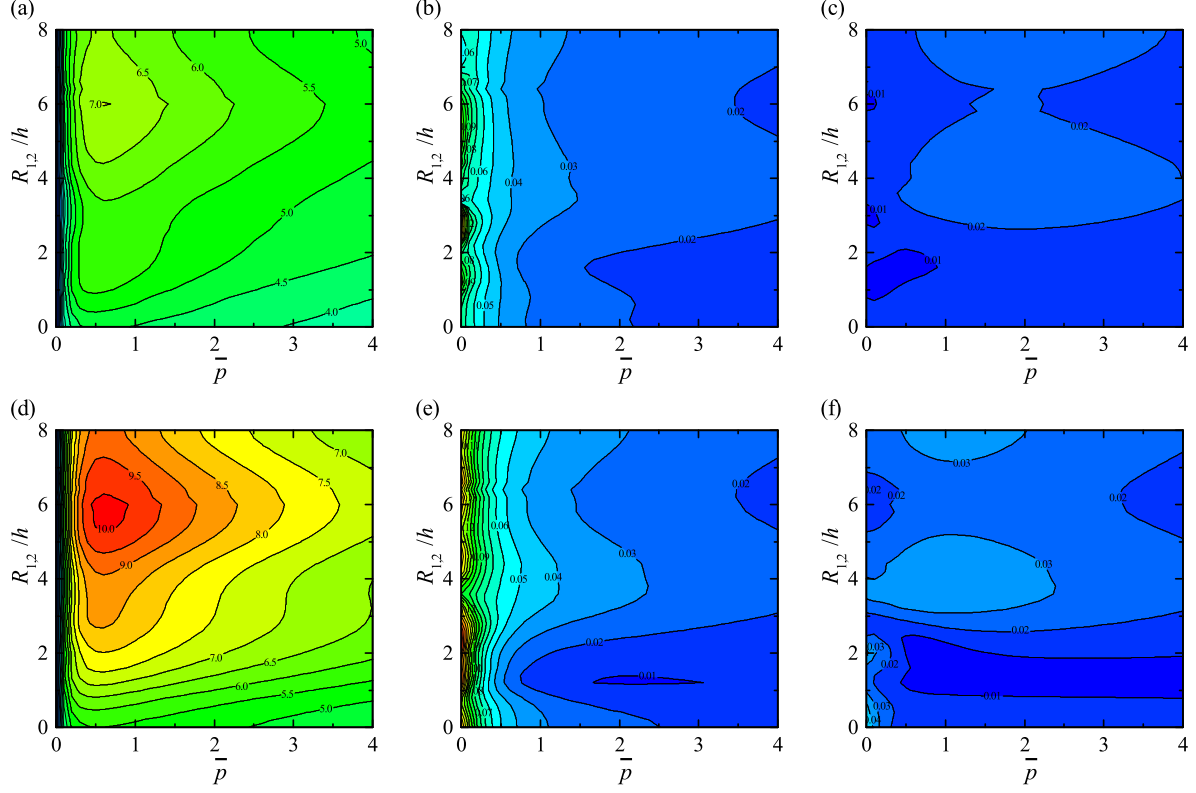


FIG. 9: Contours of wave power dissipation,  $\kappa_{diss}$  ((a) and (d)), heave excitation forces acting on plate 1,  $|F_3^{(1)}|/(\rho g \pi h^2 A)$  ((b) and (e)) and 2,  $|F_3^{(2)}|/(\rho g \pi h^2 A)$  ((c) and (f)) with the porosity parameter  $\bar{p}$  and the distance between the two plates  $R_{1,2} = x_2 - x_1$  for  $y_1 = y_2 = 0$ ,  $R/h = 2.0$ ,  $d_1/h = 0.1$ ,  $d_2/h = 0.2$ ,  $\bar{\chi} = \bar{\gamma} = 0.01$ ,  $\beta = \pi/2$  and  $kh = \pi/2$ : (a)-(c) simply supported edge conditions; (d)-(f) clamped edge conditions.

stiffness of the plates, resulting in larger wave frequencies where the peaks of the heave excitation forces occur.

Finally, in Figs. 11 and 12 we showcase the fields of the amplitude of the free surface and the amplitude of the plate deflection, respectively, for  $\bar{p} = 1.0$ ,  $\beta = \pi/2$ ,  $kh = \pi/2$ , and  $R_{1,2}/h = 0$ , 2.0, 4.0, and 6.0 with simply supported edge conditions. The waves above the plates, after shoaling into the much shallower region over the plates, undergo complicated transformation processes including the refraction and the reflection due to the phase interaction between the flows over and below the plates. In all four cases the pattern of the wave amplitude distribution obviously shows a phenomenon of wave focusing near the rear of the circular plates. The most significant of the focusing process occurs for the coaxial arrangement, i.e.,  $R_{1,2}/h = 0$  (Fig. 11a). As the two plates depart from one another horizontally, the coaxial arrangement switches into the staggered arrange-

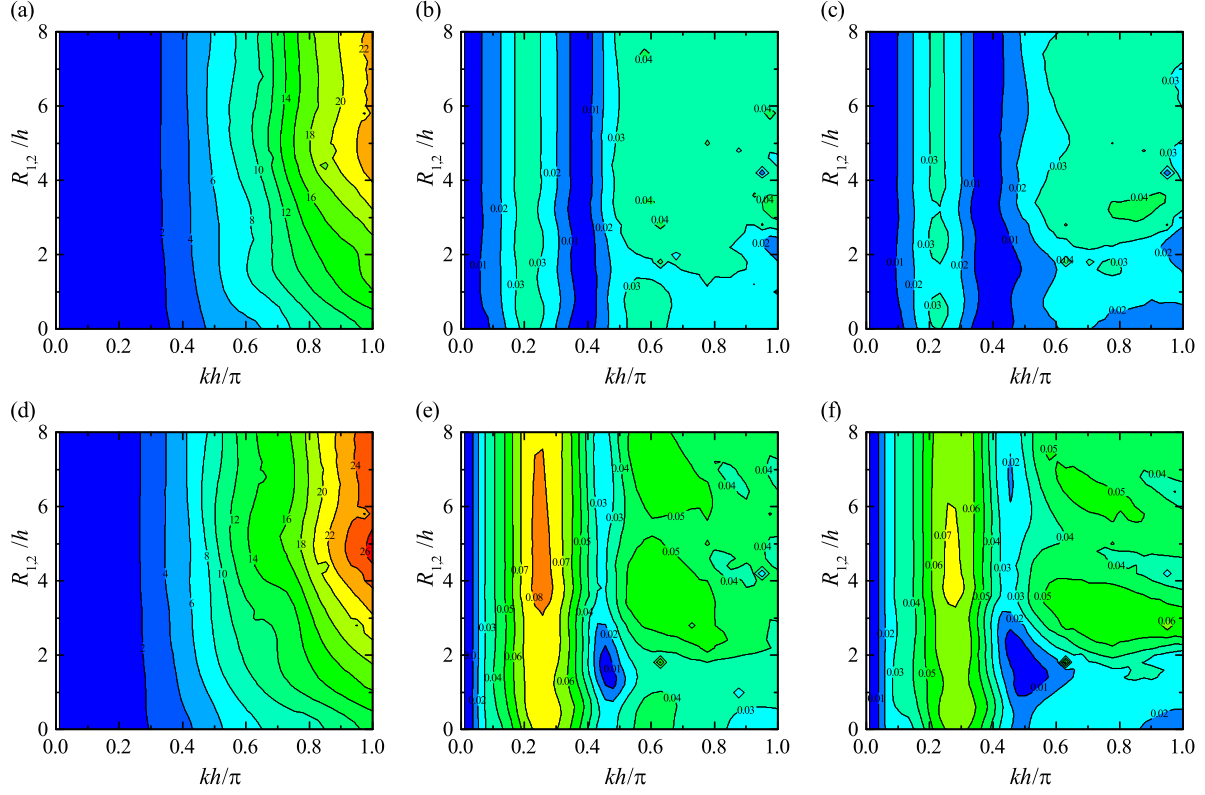


FIG. 10: Contours of wave power dissipation,  $\kappa_{diss}$  ((a) and (d)), heave excitation forces acting on plate 1,  $|F_3^{(1)}|/(\rho g \pi h^2 A)$  ((b) and (e)) and 2,  $|F_3^{(2)}|/(\rho g \pi h^2 A)$  ((c) and (f)) with the wave frequency  $kh$  and the distance between the two plates  $R_{1,2} = x_2 - x_1$  for  $y_1 = y_2 = 0$ ,  $R/h = 2.0$ ,  $d_1/h = 0.1$ ,  $d_2/h = 0.2$ ,  $\bar{\chi} = \bar{\gamma} = 0.01$ ,  $\beta = \pi/2$  and  $\bar{p} = 1.0$ : (a)-(c) simply supported edge conditions; (d)-(f) clamped edge conditions.

ment case (Fig. 11b), and the wave focusing is weakened; as the horizontal distance between the two plates is further increased, the side by side arrangement is achieved (Figs. 11c and 11d), resulting in a strengthened wave focusing. In addition to wave focusing, it is noted that there is a wave attenuation area of  $|\mathcal{E}|/A < 0.75$  surrounding the wave focusing region and extending to the leeward side of the plates. In the plotted domain, with the increase in  $R_{1,2}/h$  starting from 0, the wave attenuation area of  $|\mathcal{E}|/A < 0.75$  gets larger and separates into two regions ultimately when the arrangement becomes side by side. The strongest wave attenuation area with  $|\mathcal{E}|/A < 0.25$  is observed above the overlap region of the two plates for the coaxial and staggered arrangements (Figs. 11a and 11b). The deflection of the plates for the coaxial and staggered arrangements (Figs. 12a and 12b) is less dramatic compared to that of the side by side arrangements (Figs. 12c and 12d). This is due to the fact that the plates are both constrained at the edges, hence the fluid at

the vertical gap between the plates for the coaxial and staggered arrangements are more likely to be restricted to flow horizontally, leading to a smaller plate deformation.

To have a better understanding of the hydrodynamic characteristics of the case of stagger arrangement, the instantaneous velocity vector field at four selected cross sections, i.e.,  $x/h = 0, \pm 1$  and  $y/h = 0$ , is plotted in Fig. 13. The fluid velocity close to a sharp corner of the structure or an edge of a plate is singular, because of which the approach with special consideration of the edge singularity can achieve rapid convergence [34]. In the present model, the square-root singularity at the edge of the thin plate is incorporated by using Eq. (26). Indeed, dramatic velocities are observed at the edge of the pair of plates as shown in Fig. 13 as expected. The near field velocities at the front edges of the plates are generally stronger than those at the rear edges. The velocities of the fluid at the region around  $(x/h, y/h) = (0, 0)$ , where the two plates overlap one another, are relatively weak due to the restriction effect of the plates. Similar effect is also observed on the free surface oscillation as plotted in Fig. 11b.

Distribution of the maximum principal strain  $\epsilon_{max}^{(n)}$  is plotted in Fig. 14. The  $\epsilon_{max}^{(n)}$  is found to be relatively small at the simply supported edge, especially at the front and rear segments. For the plate submerged at a shallower depth (Plate 1), the central region of the plate closer to the rear edge is found to be another region with small principal strain, where for some particular points the principal strain ( $\epsilon_{max}^{(1)} < 0.5$ ) is even smaller than that observed at the edge. The largest principal strain ( $\epsilon_{max}^{(1)} > 3.5$ ) occurs at the front region of Plate 1. It predicts the region where the fracture and breakup of the plate are likely to happen.

## VI. CONCLUSIONS

In this paper we have considered water wave interaction with an array of submerged circular plates. The plates can be rigid/elastic and impermeable/perforated. The main focus of the paper has been to develop a theoretical model based on the linear potential flow theory and the Hankel transform to study the wave scattering by an array of circular plates. The superiority over the eigenfunction matching method is that the plates can be deployed arbitrarily without any specific limit, i.e., the arrangement could be coaxial, staggered, or side by side. The velocity potential jump across each plate is expressed as a Fourier-Gegenbauer series composed of Fourier series in the circumferential direction and Gegenbauer polynomial in the radial direction. The Gegenbauer polynomial resolves the square-root behavior at the edge of the plate resulting in rapid

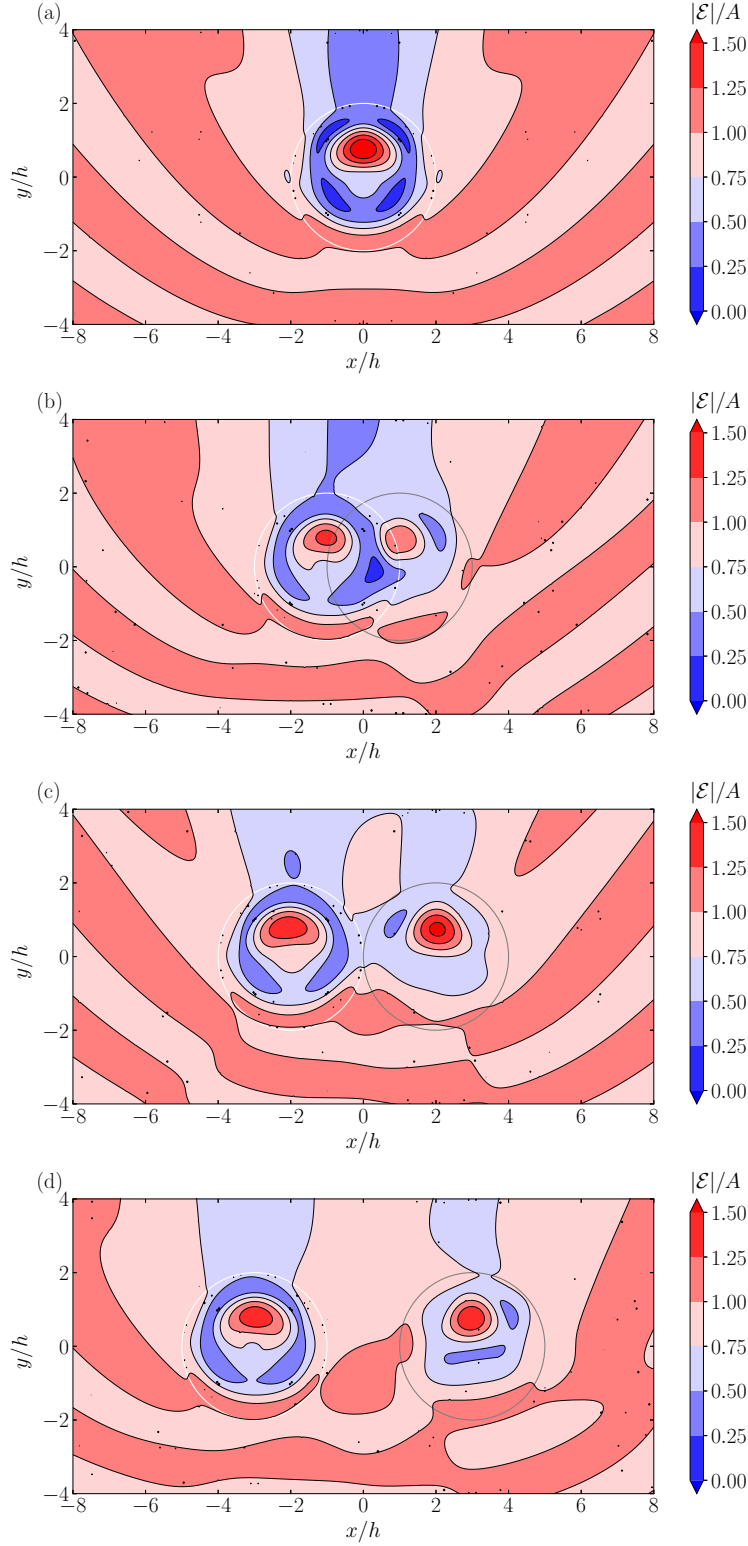


FIG. 11: Contour of the wave amplitude above a pair of elastic perforated circular plates, simply supported edge conditions,  $R_{1,2} = x_2 - x_1$  for  $y_1 = y_2 = 0$ ,  $R/h = 2.0$ ,  $d_1/h = 0.1$ ,  $d_2/h = 0.2$ ,  $\bar{\chi} = \bar{\gamma} = 0.01$ ,  $\bar{p} = 1.0$ ,  $\beta = \pi/2$  and  $kh = \pi/2$ : (a)  $R_{1,2} = 0$ , i.e., coaxial; (b)  $R_{1,2}/h = 2.0$ , i.e., staggered; (c)  $R_{1,2}/h = 4.0$ ; (d)  $R_{1,2}/h = 6.0$ , i.e., side by side.

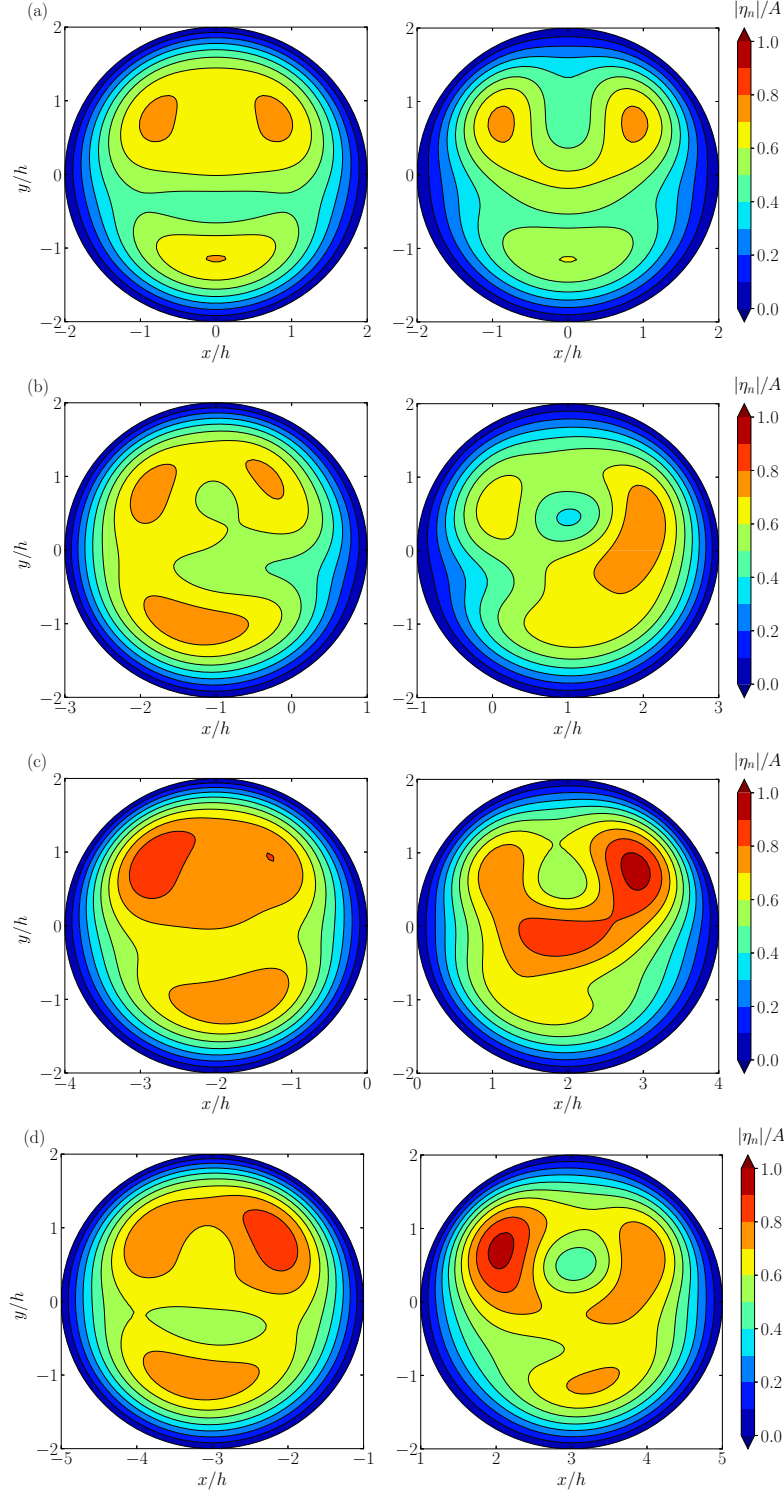


FIG. 12: Contour of the deflection of a pair of submerged elastic perforated circular plates, simply supported edge conditions,  $R_{1,2} = x_2 - x_1$  for  $y_1 = y_2 = 0$ ,  $R/h = 2.0$ ,  $d_1/h = 0.1$ ,  $d_2/h = 0.2$ ,  $\tilde{\chi} = \tilde{\gamma} = 0.01$ ,  $\bar{p} = 1.0$ ,  $\beta = \pi/2$  and  $kh = \pi/2$ : (a)  $R_{1,2} = 0$ , i.e., coaxial; (b)  $R_{1,2}/h = 2.0$ , i.e., staggered; (c)  $R_{1,2}/h = 4.0$ ; (d)  $R_{1,2}/h = 6.0$ , i.e., side by side.

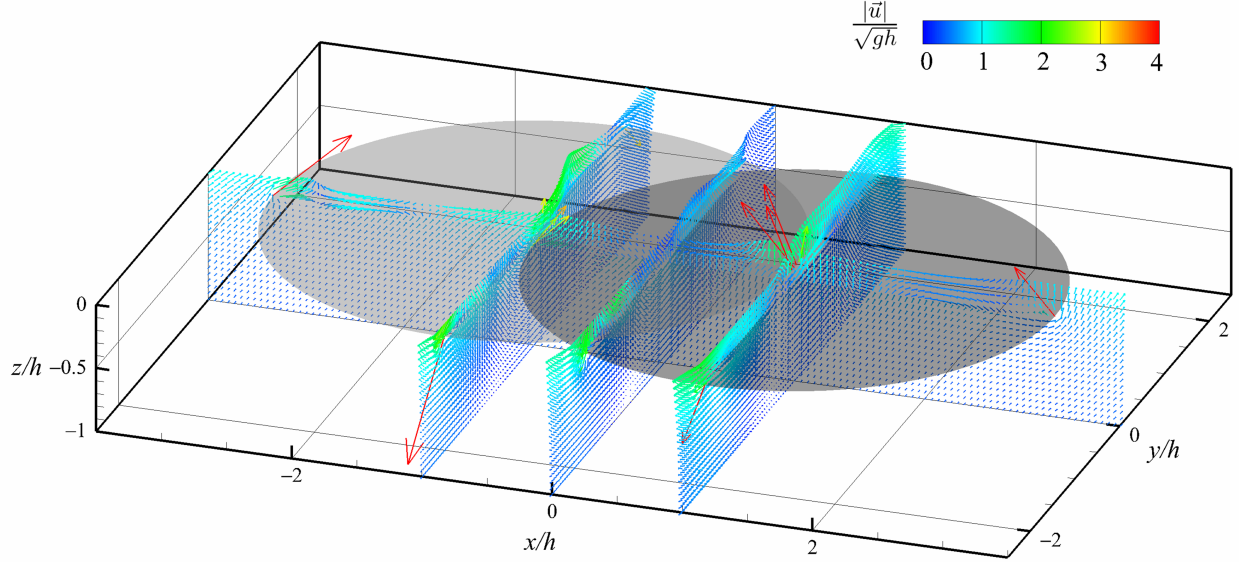


FIG. 13: The instantaneous velocity vector field around a pair of submerged elastic perforated circular plates with simply supported edge conditions at  $x/h = 0, \pm 1$  and  $y/h = 0$  for  $t = 0$ ,  $y_1 = y_2 = 0$ ,  $R/h = 2.0$ ,  $d_1/h = 0.1$ ,  $d_2/h = 0.2$ ,  $\bar{\chi} = \bar{\gamma} = 0.01$ ,  $\bar{p} = 1.0$ ,  $\beta = \pi/2$ ,  $kh = \pi/2$  and  $R_{1,2}/h = 2.0$ , i.e., the staggered arrangement corresponding to Figs. 11b and 12b.

convergence. Apart from evaluating the wave power dissipation with a straightforward method, an indirect method is derived with the employment of the Kochin functions.

Results are tested against the numerical results [33] for wave scattering by a pair of rigid impermeable circular plates, and good agreement is reached as expected. Results are also compared to the eigenfunction matching method-based semi-analytical solution of a single/a pair of elastic perforated circular plates based on the work of Zheng *et al.* [12], again showing excellent agreement.

The validated model is then applied to a series of case studies of water wave interaction with a pair of submerged elastic perforated circular plates with the horizontal distance between them ranging from 0 to  $R_{1,2} = 8h$ , which covers all the three types of arrangements, i.e., coaxial, staggered, and side by side. In the computed range of  $R_{1,2}$ , the side by side arrangements are found to dissipate more wave power than the staggered and coaxial ones. The smallest heave excitation forces acting on the two plates with clamped edge conditions both occur for the staggered arrangement. From the point of view of free surface pattern, a phenomenon of wave focusing near the rear of the circular plates is observed. Meanwhile, there is a wave attenuation area surrounding



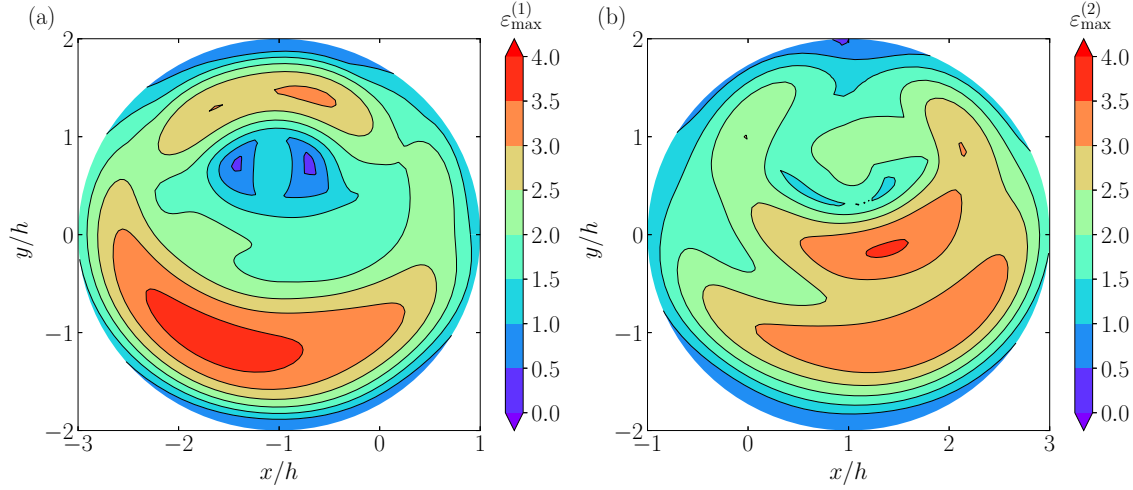


FIG. 14: Distribution of the maximum principal strain of a pair of submerged elastic perforated circular plates with simply supported edge conditions,  $R_{1,2} = x_2 - x_1$  for  $y_1 = y_2 = 0$ ,  $R/h = 2.0$ ,  $d_1/h = 0.1$ ,  $d_2/h = 0.2$ ,  $\bar{\chi} = \bar{\gamma} = 0.01$ ,  $\bar{p} = 1.0$ ,  $\beta = \pi/2$  and  $kh = \pi/2$ ,  $R_{1,2}/h = 2.0$ , i.e., the staggered arrangement corresponding to Figs. 11b, 12b, and 13.

the wave focusing region and extending to the leeward side of the plates. The strongest wave attenuation area occurs above the overlap region of the two plates for the coaxial and staggered arrangements. For the staggered arrangement, the largest normalized principal strain of the plates ( $\epsilon_{max}^{(1)} > 3.5$ ) is observed at the front region of the plate submerged at a shallower depth.

The model proposed in this paper can be easily extended to evaluate the performance of circular plate-shaped structures. An extension of the present work being considered by the current authors involves developing an array of wave energy converters, which captures wave power with the employment of either a piezoelectric power take-off (PTO) system or a conventional hydraulic/electrical linear PTO system. Another direction is to extend the present model to study wave scattering of an array of plates, some of which could float on the free surface.

## ACKNOWLEDGMENT

The research was supported by Open Research Fund Program of State Key Laboratory of Hydropscience and Engineering (Tsinghua University) (grant no. sklhse-2021-E-02) and Open Research Fund Program of State Key Laboratory of Hydraulic Engineering Simulation and Safety (Tianjin University) (grant no. HESS-1902). S.Z. and S.M. gratefully acknowledge support from



the Supergen ORE Hub ECR Research Fund project ECRRF2021-12 - “Analytical and experimental modelling of a floating/submerged elastic disk”. H.L. was supported by A\*STAR under its RIE 2020 Industry Alignment Fund, Grant No. A19F1a0104. D.G. gratefully acknowledges the EPSRC for supporting part of this work through the Supergen ORE Hub, EP/S000747/1. S.Z. wishes to thank Prof. Richard Porter from University of Bristol for valuable discussions.

### Appendix A: Choice of the integration path at $\alpha = k$

In Eq. (21), there is a pole along the integration path at  $\alpha = k$ , and we have three selections as illustrated in Fig. 15. Each choice corresponds to a specific scenario. Thus, Eq. (21) can be rewritten as

$$\phi_{n,m}(r_n, z) = \oint_0^\infty \alpha \bar{P}_{n,m}(\alpha) f_n(\alpha, z) J_m(\alpha r_n) d\alpha + \varepsilon \chi_{n,m} J_m(kr_n), \quad (\text{A1})$$

where  $\varepsilon = -1, 0$ , and  $1$ , which correspond to the integrating paths along  $L_1, L_2$ , and  $L_3$ , respectively, and

$$\chi_{n,m} = \frac{i\pi k \sinh[k(h - d_n)] \cosh[k(z + h)] \bar{P}_{n,m}(k)}{2hN_0}, \quad (\text{A2})$$

with

$$N_0 = \frac{1}{2} \left( 1 + \frac{\sinh(2kh)}{2kh} \right). \quad (\text{A3})$$

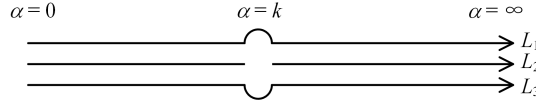


FIG. 15: Three integration paths across the pole.

The asymptotic forms for the Bessel functions with  $r_n \rightarrow \infty$  are

$$\begin{aligned} J_m(\alpha r_n) &\sim \sqrt{\frac{2}{\alpha r_n}} \cos\left(\alpha r_n - \frac{m\pi}{2} - \frac{\pi}{4}\right) \\ &= \sqrt{\frac{2}{\alpha r_n}} \left\{ \cos\left(kr_n - \frac{m\pi}{2} - \frac{\pi}{4}\right) \cos[(\alpha - k)r_n] - \sin\left(kr_n - \frac{m\pi}{2} - \frac{\pi}{4}\right) \sin[(\alpha - k)r_n] \right\}. \end{aligned} \quad (\text{A4})$$

Further, we have the following two formulations

$$\begin{aligned}
& \int_0^\infty \sqrt{\frac{2}{\alpha r_n}} \alpha \bar{P}_{n,m}(\alpha) f_n(\alpha, z) \cos[(\alpha - k)r_n] d\alpha \\
&= \left( \int_0^{k-\varepsilon} + \int_{k+\varepsilon}^\infty \right) \sqrt{\frac{2\alpha}{r_n}} \bar{P}_{n,m}(\alpha) f_n(\alpha, z) (\alpha - k) \frac{\cos[(\alpha - k)r_n]}{\alpha - k} d\alpha \\
&\leq \max \left[ \sqrt{2\alpha} \bar{P}_{n,m}(\alpha) f_n(\alpha, z) (\alpha - k) \right] \sqrt{\frac{1}{r_n}} \left( \int_0^{k-\varepsilon} + \int_{k+\varepsilon}^\infty \right) \frac{\cos[(\alpha - k)r_n]}{\alpha - k} d\alpha \quad (\text{A5}) \\
&= \max \left[ \sqrt{2\alpha} \bar{P}_{n,m}(\alpha) f_n(\alpha, z) (\alpha - k) \right] \sqrt{\frac{1}{r_n}} \left( \int_{-kr_n}^{-\varepsilon r_n} + \int_{\varepsilon r_n}^\infty \right) \frac{\cos x}{x} dx \\
&\sim O\left(r_n^{-1.5}\right),
\end{aligned}$$

and

$$\begin{aligned}
& \int_0^\infty \sqrt{\frac{2}{\alpha r_n}} \alpha \bar{P}_{n,m}(\alpha) f_n(\alpha, z) \sin[(\alpha - k)r_n] d\alpha \\
&= \left( \int_{k-\varepsilon}^{k+\varepsilon} + \int_0^{k-\varepsilon} + \int_{k+\varepsilon}^\infty \right) \sqrt{\frac{2}{\alpha r_n}} \alpha \bar{P}_{n,m}(\alpha) f_n(\alpha, z) (\alpha - k) \frac{\sin[(\alpha - k)r_n]}{\alpha - k} d\alpha \\
&= \sqrt{\frac{2}{kr_n}} \frac{\chi_{n,m}}{i\pi} \int_{k-\varepsilon}^{k+\varepsilon} \frac{\sin[(\alpha - k)r_n]}{\alpha - k} d\alpha + O\left(r_n^{-1.5}\right) \quad (\text{A6}) \\
&= 2\sqrt{\frac{2}{kr_n}} \frac{\chi_{n,m}}{i\pi} \int_0^{\varepsilon r_n} \frac{\sin x}{x} dx + O\left(r_n^{-1.5}\right) \\
&\sim -i\sqrt{\frac{2}{kr_n}} \chi_{n,m} + O\left(r_n^{-1.5}\right),
\end{aligned}$$

because [e.g., see 26]

$$\text{si}(x) = - \int_x^\infty \frac{\sin \alpha}{\alpha} d\alpha \sim -\frac{\cos x}{x}, \quad x \rightarrow \infty, \quad (\text{A7})$$

and

$$\text{Ci}(x) = - \int_x^\infty \frac{\cos \alpha}{\alpha} d\alpha \sim \frac{\sin x}{x}, \quad x \rightarrow \infty. \quad (\text{A8})$$

With the employment of Eqs. (A4)-(A6),  $\phi_{n,m}(r_n, z)$  with  $r_n \rightarrow \infty$  can be expressed as

$$\begin{aligned}
\phi_{n,m}(r_n, z) &\sim \chi_{n,m} \sqrt{\frac{2}{kr_n}} \left[ i \sin \left( kr_n - \frac{m\pi}{2} - \frac{\pi}{4} \right) + \varepsilon \cos \left( kr_n - \frac{m\pi}{2} - \frac{\pi}{4} \right) \right] \\
&= \begin{cases} -\sqrt{\frac{2}{kr_n}} e^{-i(kr_n - \frac{m\pi}{2} - \frac{\pi}{4})} \chi_{n,m}, & \varepsilon = -1, \text{ i.e., path } L_1 \\ i\sqrt{\frac{2}{kr_n}} \sin(kr_n - \frac{m\pi}{2} - \frac{\pi}{4}) \chi_{n,m}, & \varepsilon = 0, \text{ i.e., path } L_2 \\ \sqrt{\frac{2}{kr_n}} e^{i(kr_n - \frac{m\pi}{2} - \frac{\pi}{4})} \chi_{n,m}, & \varepsilon = 1, \text{ i.e., path } L_3 \end{cases} \quad (\text{A9})
\end{aligned}$$

Accounting for the time-harmonic oscillator  $e^{-i\omega t}$ , the integration paths  $L_1$ ,  $L_2$  and  $L_3$  correspond to the inwards propagating waves, standing waves, and outwards propagating waves, respectively. To ensure that the diffracted waves are outgoing, the contour of integration is defined to bypass the pole  $\alpha = k$  from below, i.e., the integrating path along  $L_3$  and  $\varepsilon = 1$ .

- 
- [1] Stamnes JJ, Løvhaugen O, Spjelkavik B, Mei CC, Lo E, Yue DKP. 1983 Nonlinear focusing of surface waves by a lens—theory and experiment. *J. Fluid Mech.*, **135**, 71–94.
  - [2] Molin B. 2011 Hydrodynamic modeling of perforated structures. *Appl. Ocean Res.*, **33**, 1–11.
  - [3] Michele S, Buriani F, Renzi E, van Rooij M, Jayawardhana B, Vakis AI. 2020 Wave energy extraction by flexible floaters. *Energies*, **13**, 6167.
  - [4] Michele S, Zheng S, Greaves D. 2022 Wave energy extraction from a floating flexible circular plate. *Ocean Eng.*, **245**, 110275.
  - [5] Zheng S, Michele S, Liang H, Meylan MH, Greaves D. 2022 Wave power extraction from a floating elastic disk-shaped wave energy converter. *J. Fluid Mech.*, **948**, A38.
  - [6] Liang H, Zheng S, Magee A, Greaves D. 2022 Water wave interactions with perforated elastic disks: Quadratic pressure discharge condition. *Phys. Rev. Fluids*, **7**, 054802.
  - [7] Renzi E, Michele S, Zheng S, Jin S, Greaves D. 2021 Niche applications and flexible devices for wave energy conversion: A review. *Energies*, **14**, 6537.
  - [8] Meylan MH, Squire VA. 1996 Response of a circular ice floe to ocean waves. *J. Geophys. Res.*, **101**, 8869–8884.
  - [9] Bottom II RG, Borazjani I, Blevins EL, Lauder GV. 2016 Hydrodynamics of swimming in stingrays: numerical simulations and the role of the leading-edge vortex. *J. Fluid Mech.*, **788**, 407–443.
  - [10] Mahmood-Ul-Hassan, Meylan MH, Peter MA. 2009 Water-wave scattering by submerged elastic plates. *Q. J. Mech. Appl. Math.*, **62**, 321–344.
  - [11] Zheng S, Meylan MH, Zhu G, Greaves D, Iglesias G. 2020 Hydroelastic interaction between water waves and an array of circular floating porous elastic plates. *J. Fluid Mech.*, **900**, A20.
  - [12] Zheng S, Meylan MH, Greaves D, Iglesias G. 2020 Water-wave interaction with submerged porous elastic disks. *Phys. Fluids*, **32**, 047106.
  - [13] McIver P. 1998 The dispersion relation and eigenfunction expansions for water waves in a porous structure. *J. Eng. Math.*, **34**, 319–334.
  - [14] Evans DV, Peter MA. 2011 The dispersion relation and eigenfunction expansions for water waves in

- a porous structure. *J. Eng. Math.*, **69**, 135-154.
- [15] Linton CM, McIver P. 2000 *Handbook of Mathematical Techniques for Water Waves*. CRC Press, Southampton UK.
- [16] Martin PA, Llewellyn-Smith SG. 2011 Generation of internal gravity waves by an oscillating horizontal disc. *Proc. R. Soc. A*, **267**, 3406–3423.
- [17] Porter R. 2015 Linearised water wave problems involving submerged horizontal plates. *Appl. Ocean Res.*, **50**, 91–109.
- [18] Liang H, Chen XB. 2017 A new multi-domain method based on an analytical control surface for linear and second-order mean drift wave loads on floating bodies. *J. Comp. Phys.*, **347**, 506–532.
- [19] Wehausen JV, Laitone EV. 1960 Surface waves. In: *Hanbuch der Physik*. **9**, 446–778, Springer.
- [20] Farina L, Martin PA. 1998 Scattering of water waves by a submerged disc using a hypersingular integral equation. *Appl. Ocean Res.*, **20**, 121-134.
- [21] Islam N, Kundu S, Gayen R. 2019 Scattering and radiation of water waves by a submerged rigid disc in a two-layer fluid. *Proc. R. Soc. A*, **475**, 2019033.
- [22] Liang H, Chen X, Chan ES. 2021 Radiation of water waves by a heaving disc in a uniform current. *Proc. 36th International Workshop on Water Waves and Floating Bodies*, Seoul, Korea, April 25-28.
- [23] Smith MJA, Peter MA, Abrahams D, Meylan MH. 2020 On the Wiener-Hopf solution of water-wave interaction with a submerged elastic or poroelastic plate. *Proc. R. Soc. A*, **476**, 20200360.
- [24] Behera H, Sahoo T. 2015 Hydroelastic analysis of gravity wave interaction with submerged horizontal flexible porous plate. *J. Fluids Struct.*, **54**, 643–660.
- [25] Meylan MH, Bennetts LG, Peter MA. 2017 Water-wave scattering and energy dissipation by a floating porous elastic plate in three dimensions. *Wave Motion*, **70**, 240–250.
- [26] Abramowitz M, Stegun IA. 1964 *Handbook of mathematical functions with formulas, graphs, and mathematical tables*. Government Printing Office.
- [27] Zheng S, Porter R, Greaves D. 2020 Wave scattering by an array of metamaterial cylinders. *J. Fluid Mech.*, **903**, A50.
- [28] Reddy JN. 2007 *Theory and analysis of elastic plates and shells*. CRC Press.
- [29] Fung YC. 1977 *A first course in continuum mechanics*. Englewood Cliffs.
- [30] Yang YF, Wu GX, Ren K. 2022 Hydroelastic wave diffraction by a vertical circular cylinder standing in a channel with an ice cover. *J. Fluid Mech.* **941**, A13.
- [31] Falnes J. 2002 *Ocean waves and oscillating systems: linear interactions including wave-energy ex-*

*traction*. Cambridge University Press.

- [32] Porter R, Zheng S, Greaves D. 2021 Extending limits for wave power absorption by axisymmetric devices. *J. Fluid Mech.*, **924**, A39.
- [33] Liang H, Zheng S, Shao Y, Chua KH, Choo YS, Greaves, D. 2021 Water wave scattering by impermeable and perforated plates. *Phys. Fluids*, **33**, 077111.
- [34] Liang H, Faltinsen OM, Shao YL. 2015 Application of a 2D harmonic polynomial cell (HPC) method to singular flows and lifting problems. *Appl. Ocean Res.* **53**, 75-90.